Downregulation of *Trpv4* and *Klf2* in brain microvessels is associated with the progression of neurovascular dysfunction and cognitive impairment in a model of heart failure with preserved ejection fraction.

Sara M.P. Lambrichts[1,2,9], Laura van der Taelen[1,10], Irene Pastor[1], Peter Leenders[1], Nicole Bitsch[10], Daria Majcher[1,10], Denise Hermes[3,9], Steven J. Simmonds[4], Marcel van Herwijnen[6], Rick Kamps[6,9], Ellen Weltjens[1,10], Hellen P. Steinbusch[3,9], Floor Arentz[7], Maximilian Wiesmann[7], Amanda J. Kiliaan[7], Florian Caiment[6,8], Martina Kutmon[5], Elizabeth A.V. Jones[4,10], Robert J. van Oostenbrugge[2,9,10], Sébastien Foulquier[1,2,9,10]

[1] Dept of Pharmacology and Toxicology, Maastricht University, The Netherlands.

[2] Dept of Neurology, Maastricht University Medical Center, The Netherlands.

[3] Dept of Psychiatry and Neuropsychology, Maastricht University, The Netherlands.

[4] Dept of Cardiovascular Science, Centre for Molecular and Vascular Biology, KU Leuven, Belgium.

[5] Maastricht Centre for Systems Biology and Bioinformatics (MaCSBio), Maastricht University, The Netherlands.

[6] Dept of Translational genomics, Maastricht University, The Netherlands.

[7]Department of Medical Imaging, Anatomy, Research Institute for Medical Innovation, Radboud University Medical Center, Donders Institute for Brain, Cognition & Behaviour, Preclinical Imaging Center PRIME, Radboud Alzheimer Center, Nijmegen, the Netherlands.

[8] GROW – Research institute for Oncology and Reproduction, Maastricht University, The Netherlands.

[9] MHeNS – Research institute of Mental Health and Neuroscience, Maastricht University, The Netherlands.

[10] CARIM – Research institute of Cardiovascular Diseases, Maastricht University, The Netherlands.

Corresponding author

Sébastien Foulquier, Pharm.D., Ph.D.

Maastricht University, Dept of Pharmacology-Toxicology

Universiteitssingel 50, P.O. Box 616,

6200 MD Maastricht, The Netherlands

s.foulquier@maastrichtuniversity.nl

ABSTRACT

198/200 words

Vascular cognitive impairment (VCI) shares major risk factors with heart failure with preserved ejection fraction (HFpEF), including obesity, diabetes and hypertension. Yet VCI research often relies on single-stimulus models, whereas patients experience combined risk factors. We therefore assessed cerebrovascular and cognitive phenotypes in an HFpEF model and investigated underlying mechanisms.

Male Lean and Obese ZSF1 rats underwent longitudinal assessments of blood pressure, glucose, cardiac function, and behavioural performance. Cerebral blood flow and neurovascular coupling were assessed by laser speckle contrast imaging. White matter integrity, blood–brain barrier (BBB) permeability, and vascular density were analysed by (immuno)histochemistry. Cortical microvessels were isolated for transcriptomic profiling, and selected targets were validated using multiplex in-situ hybridization.

Obese rats exhibited neurovascular uncoupling and impaired short- and long-term memory and spatial learning, accompanied by brain atrophy and reduced myelin. BBB permeability increased at 22-23 weeks and vascular density at 34-35 weeks in Obese vs Lean rats. Transcriptomic analysis of brain microvessels revealed altered processes related to angiogenesis, vasoreactivity, immune mechanisms and vascular remodelling, with consistent downregulation of *Trpv4* and *Klf2*.

Obese ZSF1 rats develop progressive neurovascular dysfunction associated with HFpEF onset and reduced *Trpv4* and *Klf2* expression in cerebral microvessels, two key vasoprotective genes.

Keywords: Diastolic dysfunction, Cerebral small vessel disease, Microvascular dysfunction, Cerebrovascular reactivity, *Trpv4*, *Klf2*.

54 # INTRODUCTION

55 From all dementia cases, more than 20% of the patients are diagnosed with vascular cognitive
56 impairment (VCI). This mental disease covers all cognitive disorders caused by vascular dysfunction
57 ranging from mild cognitive impairment to frank dementia (1). The most common cause of VCI is
58 cerebral small vessel disease (cSVD), an umbrella term that covers all pathologies affecting cerebral
59 microvessels and of which age and cardiovascular risk factor related cSVD is the most common form.
60 This later type is characterized by white matter lesions, cerebral microbleeds, enlarged perivascular
61 spaces, lacunar infarct, and brain atrophy (2). A systematic review and meta-analysis demonstrated
62 that the presence of lacunes, white matter lesions and cerebral microbleeds are associated with left
63 ventricular hypertrophy, highlighting a link between heart and brain disorders (3). Interestingly, the
64 development of both VCI and heart failure are strongly linked to the presence of comorbidities such as
65 obesity, diabetes, aging and hypertension (4). The brain and heart are especially sensitive to the
66 chronic effect of comorbidities because of their high energetic and metabolic demands (5). With a
67 growing aging population and the high prevalence of vascular risk factors in elderly, the incidence of
68 VCI and heart failure is expected to further rise in the coming decades (6, 7).

69 Current evidence indicates that cognitive function declines more rapidly in patients with heart
70 failure and that it may be affected prior to heart failure diagnosis (8). Two types of heart failure can be
71 distinguished: heart failure with reduced ejection fraction (HFrEF), which is linked to the loss of
72 cardiomyocytes caused by for instance ischemia or myocarditis; and heart failure with preserved
73 ejection fraction (HFpEF), which is preceded by chronic comorbidities resulting in left ventricular
74 hypertrophy and diastolic dysfunction (9).

75 Microvascular dysfunction has been proposed as a potential common mechanism for the
76 development of cardiac and cognitive disorders (5). Although this process manifests differently in each
77 organ, microvascular dysfunction can generally be defined as an altered structure of the

78 microvasculature, such as vascular remodelling or rarefaction; and/or an altered function, including
79 increased microvascular resistance and deregulation of vascular tone in reaction to stimuli, ultimately
80 leading to hypoperfusion of the affected organs (10). Recent findings demonstrate that the coronary
81 flow reserve is impaired in 50% of patients that present with coronary microvascular dysfunction (11).
82 Moreover, the integrity of the microvascular wall barrier was found to be affected in HFpEF-associated
83 comorbidities, thereby contributing to increased permeability of the endothelium. In case of cSVD
84 patients, blood-brain barrier (BBB) impairment and cerebral hypoperfusion have been found to be
85 strongly correlated with white matter lesions (12). Both cerebral blood flow and the BBB are controlled
86 by cells of the neurovascular unit (13). To ensure the high energetic and metabolic demand of the
87 brain, proper neurovascular coupling is essential. However, when this process becomes impaired, the
88 metabolic demands of neurons cannot be fulfilled, subsequently leading to neurodegeneration and
89 cognitive decline (2).

90 At present, no targeted therapeutic options are available for VCI nor HFpEF. Life quality of patients
91 can only be improved by treating the associated comorbidities (6, 14). Although the underlying
92 pathological mechanism of both disorders remains elusive, a central role for chronic hypoperfusion or
93 impaired vascular reactivity through endothelial dysfunction has been proposed (5, 11). Moreover,
94 recent findings demonstrated a reduced oxygenation reserve in myocardial and cerebral vasculature
95 of patients with heart failure (5). Taken together, studies are highlighting microvascular dysfunction as
96 an essential element of VCI in heart failure, but the mechanisms underlying this dysfunction remain
97 largely unknown.

98 In this study, we aimed to characterize the cognitive and cerebrovascular phenotype in a rat model
99 of HFpEF and to investigate the molecular processes governing the development of VCI in HFpEF. We
100 performed a longitudinal study to assess the effect of comorbidities (obesity, diabetes, hypertension)
101 on cerebral blood flow, neurovascular coupling, vascular density and BBB integrity at key time points
102 associated with the disease progression. Furthermore, we assessed the dynamic transcriptomic

103 regulations within cortical brain microvessels and validated *Trpv4* and *Klf2* as important signalling
104 elements for the development of VCI in this HFpEF model.

105 METHODS

106 1. Animals and study design

107 All experiments and procedures within this study were conducted in accordance with institutional
108 and ARRIVE guidelines and approved by the local (Maastricht University IvD, DEC-UM) and national
109 (CCD) ethical Committees for Animal Experiments (AVD10700202010326). ZSF1 rats and Wistar rats
110 were obtained from Charles River Inc. and Janvier Labs, respectively. Obese ZSF1 rats are known to
111 develop hypertension, obesity, diabetes and heart failure with preserved ejection fraction (HFpEF),
112 whereas Lean animals present with only hypertension (15). The cognitive and cardiovascular pheno-
113 type of the ZSF1 rats was studied at an early time point before the development of HFpEF (14-16w in
114 Study 1, 6-7w in Study 2, a middle time point (20-22w) where Obese ZSF1 present with HFpEF, and a
115 late time point of prolonged exposure to comorbidities (30-32w) (16). In addition, Wistar rats (20-
116 22w) were included in Study 2 to compare parameters such as cerebral blood flow measurements to
117 reference values from normotensive rats.

118 Animals were socially housed in a 12/12-h reversed light/dark cycle (lights on from 19:00 to 7:00h),
119 except during the novel objection recognition task (NORT, section 0). Cage locations within the housing
120 rooms were randomized at the start of the experiments and at regular intervals during the study to
121 minimize location bias. A radio played softly, providing background noise 24h a day, also during testing.
122 Rats had free access to sterilized tap water and food; breeding diet (v1124-703, SSNIFF Spezialdiäten
123 GmbH) for ZSF1 rats and standard diet (v1534-703, SSNIFF Spezialdiäten GmbH) for Wistar rats. Body
124 weights were measured weekly. Due to the obvious difference in size/body weight between Obese
125 and Lean animals, the investigators were aware of the group allocation during the execution of the
126 studies. However, data sets were anonymized for all image analyses.

127 *Study 1*

128 Lean and Obese ZSF1 rats (n_{Lean}=15, n_{Obese}=14) were subjected to a series of behavioural testing to
129 assess vascular cognitive impairment (VCI) at 14-16, 20-22 and 30-32 weeks old. Every two weeks,
130 blood was collected via the *vena saphena* and fasted blood glucose (FBG) was measured (section 2).
131 At 33-34 weeks old, thinned skull window surgeries (section 5) were performed to measure cerebral
132 blood flow and assess neurovascular coupling using laser speckle contrast imaging (LSCI, PeriCam PSI
133 HR, Perimed). At time of sacrifice, blood was collected from the *vena cava*. Isolated rat brains were cut
134 sagitally and prepared for cortical brain microvessel isolation (section 10.1) and immunohistochemistry
135 (section 0) respectively.

136 *Study 2*

137 The cardiovascular phenotype of Lean and Obese ZSF1 rats (n=14/group) was assessed in a
138 longitudinal study during which blood pressure and echocardiography measurements were performed
139 at the age of 6-7w, 20-21w and 30-31w. Every five weeks, blood was collected and FBG was measured.
140 Thinned skull window surgeries and LSCI were performed on Lean and Obese rats at 6-7, 20-21 and 32-
141 33 weeks old, as well as on normotensive Wistar rats (n=12, 20-21w). At time of sacrifice, blood was
142 collected via *vena cava*. After isolation, rat brains were sagitally cut and used for cortical brain
143 microvessel isolation (section 10.1) and immunohistochemistry (section 0) respectively.

144 ## 2. Glucose measurement

145 Animals were fasted for 6h in cages with paper bedding. Blood was collected from the *vena*
146 *saphena* using EDTA-precoated tubes (Microvette CB 300, Fisher Scientific, 16.444.100) during the
147 active phase of the animals (14:00 to 16:00h). Briefly, glucose was measured using a Contour glucose
148 meter (Ascensia Diabetes) and Contour test strips (Ascensia Diabetes, 84638099). Blood samples were
149 kept on ice until the end of the procedure, followed by centrifugation at 2000 g for 10 minutes at 4°C.
150 Plasma was then stored at -80°C until further use.

151 ## 3. Assessment of the cardiovascular phenotype

152 Blood pressure and cardiac function were determined in Lean and Obese ZSF1 rats (n=14/group)
153 at three disease stages. Systolic and diastolic blood pressures were measured in awake rats during
154 their active phase with the CODA tail-cuff system (Kent Scientific corporation) using volume pressure
155 recording. Prior to start of the experiment, animals were habituated to a restrainer for 15 minutes in
156 a warming cabinet (28°C) for three consecutive days. At least 20 continuous blood pressure
157 measurements were recorded and averaged for each rat.

158 During echocardiography, rats were anaesthetized with an i.p. injection of ketamine (75-100
159 mg/kg, Ketamine 10%, Alfasan) and xylazine (7.5-10 mg/kg, Xylasan 2%, Alfasan) dissolved in 0.9% NaCl
160 (Baxter). All measurements were conducted according to previously described methods in Cuijpers et
161 al. 2020 (16). During measurement, animals were placed in supine position and body temperature was
162 monitored using a rectal probe and maintained at 37°C using a heating path and lamp. Heart and
163 breathing rate were monitored via echocardiogram recording. A MS250 transducer (12.5-45 MHz)
164 connected to Vevo 2100 echocardiography (VisualSonics) was used for 2D B- and M-mode imaging,
165 pulse wave and tissue Doppler imaging. Left ventricle wall thickness was measured in B- and M-mode
166 of parasternal short axis at the level of papillary muscles. Pulse wave Doppler measurements were
167 performed to acquire pulmonary and aortic peak velocities in apical four-chamber view. Lastly,
168 diastolic dysfunction was assessed by pulse wave and tissue Doppler imaging of the mitral valve. After
169 the procedure, anaesthetized animals were awakened with atipamezole (i.p., 0.1 mg/kg). Vevo 2100
170 1.6.0 Software (VisualSonics) was used to extract functional parameters and perform analyses. Values
171 of three stable cardiac cycles were averaged for each parameter.

172 ## 4. Behavioural testing

173 *Elevated zero maze*

174 Anxiety of ZSF1 rats was assessed with the EZM in dark conditions. Rats were placed in the middle
175 of an open arm to facing one of the closed arms and allowed to explore the maze over a period of five

176 minutes. The total duration and distance travelled in the open and closed parts were measured via an
177 infrared video camera connected to a video tracking system (Ethovision Pro, Noldus). Analysis was
178 accomplished in Ethiovision XT15 (Ethovision Pro, Noldus).

179 *Y-maze*

180 The YM alternation task was performed to investigate spatial working memory in similar conditions
181 as the EZM. Animals were placed in one of the three arms and allowed to explore the maze over a
182 period of six minutes. The number of arm entries per animal was counted, and the alternation rate
183 was used as a measure for working memory. Animals with a proper working memory have an
184 alternation rate significantly above the 50% chance level. In addition, the total distance travelled in the
185 YM was measured via an infrared video camera connected to a video tracking system and analysed in
186 Ethiovision XT15. Animals with less than five arm entries were excluded from the dataset.

187 *Novel object recognition task*

188 Short-term memory of ZSF1 rats was evaluated using the NORT. Animals were housed individually
189 two days prior to testing until the final testing day of the NORT (17). The test was performed in dark
190 conditions and animals were familiarized to the arena and objects during two training days. On the
191 two testing days, a first trial (T1) was performed with two identical objects. After a 1h-interval, animals
192 were subjected to a second trial (T2) where one of the two objects was replaced by a novel object.
193 Both trials lasted three minutes and animals returned to their home cage after the first trial. Total
194 exploration time was monitored during testing: exploration of the objects by the animals was
195 represented by looking, licking, sniffing or touching the objects while sniffing. Any rat exploring less
196 than five and eight seconds during T2 of the first and second testing day respectively was excluded
197 from the study. The discrimination index d2 during the first minute of the test was used as a measure
198 for short-term spatial memory and is expressed as the difference between the time spent to the new
199 and old object in T2 divided by the total exploration time in T2. Proper short-term memory is
200 considered when d2 is significantly above 0.

201 *Barnes maze*

202 Assessment of long-term spatial learning and memory was done during a five-day testing period
203 in an adapted BM task (18). The experiment was performed under light conditions and a maximum of
204 six rats was allowed to habituate to the testing environment for 15 minutes prior to the start. During
205 the four training days, ZSF1 rats were subjected to four trials a day with each rat being allocated to a
206 different target arm. The trial ended after three minutes or when the animal entered the correct target
207 arm. On the last day of the BM, a probe trial was performed in which the animal remained in the arena
208 for three minutes. The relative time spent in the target quadrant during the first 30 seconds of the trial
209 was used as a measurement for long-term memory. Lastly, a reversed learning trial was performed in
210 which each rat was assigned to a different arm than during the training days to assess reversal learning.
211 The total duration and distance travelled until reaching the correct target arm was measured with a
212 video camera connected to a video tracking system. Analysis was done in Ethiovision XT15.

213 5. Thinned skull window surgeries and laser speckle contrast imaging

214 Animals underwent thinned skull window surgeries to assess cerebral blood flow and
215 neurovascular coupling. One hour following carprofen injection (s.c., 5 mg/kg, Rimadyl), rats were
216 anaesthetized using 2.5-3.5% isoflurane (IsoFlo, Zoetis) and fixed in a stereotactic frame. During
217 surgery, body temperature was monitored using a rectal probe and maintained at 37°C using a heating
218 path and lamp. Before midline incision, 2% lidocaine (Fresenius Kabi AG) was injected onto the
219 periosteum. The region above the left barrel cortex (5.5-6 mm lateral and 2.5 mm posterior to Bregma)
220 was thinned using a high-speed microdrill (NSK Euope, Mio 35M) under a stereo microscope (Leica
221 MZ8, Leica Microsystems). After completing the skull-thinning, animals were injected with 0.05-1
222 mg/kg medetomidine (s.c., SedaSTART, ASTfarma) to maintain a light sedation state. To keep the skull
223 hydrated and improve image quality, light mineral oil (0.838 g/ml, Sigma Aldrich, 330779) and heavy
224 mineral oil (0.862 g/ml, Sigma Aldrich, 330760) were subsequently added on top of the thinned
225 window. After a 20-minute isoflurane washout period, whisker stimulation was performed by

226 mechanically shaking the whiskers for 30 seconds at a frequency of 5 Hz on the contralateral side of
227 the thinned skull window. The stimulation was done using a home-made stepper-motor system
228 connected to a foam brush and controlled by an Arduino board. Stimulation was repeated three times
229 with a two-minute interval and images were acquired at baseline before and during stimulation via
230 LSCI (resolution = 10 µm, image size = 5 x 5 mm; frame averaging = 10; frame rate = 44 images/second).
231 After measurements, animals were s.c. injected with saline and atipamezole (Antisedan, Orion
232 Corporation) to end sedation. All rats received carprofen (5 mg/kg) in their drinking water and were
233 checked daily until three days post-surgery.

234 Analysis was accomplished using PIMSoft 1.11 software (Perimed); three regions of interest (0.1 x
235 0.1 mm) were selected in the barrel cortex area. Neurovascular coupling was relatively expressed to
236 the average baseline cerebral blood flow prior to each whisker stimulation. Three values were
237 averaged per animal.

238 6. Sample collection

239 One hour prior to sacrifice, rats were injected with 0.05 mg/kg buprenorphine (s.c., Bupaq,
240 Fendigo, Pharma AG). Briefly, animals were anaesthetized with 4% isoflurane and blood was
241 withdrawn from the *vena cava*, followed by pentobarbital injection (i.v., 100 mg/kg, Nembutal, Ceva)
242 and cardiac perfusion with ice-cold PBS supplemented with 1% EDTA (pH 8.0, ThermoFisher,
243 15575020). Organs, plasma and urine samples were prepared for further analyses and either snap
244 frozen in liquid nitrogen or fixed in 4% paraformaldehyde (PFA, Sigma-Aldrich, 158127), washed with
245 PBS and stored in PBS with 0.1% sodium azide (Sigma Aldrich, 26628-22-8). In addition, brains and
246 hearts were weighted on a precision scale (Mettler Toledo, XP603S), whereas tibia length was
247 measured using a vein caliper.

248 7. Plasma molecular analysis

249 During terminal procedure, blood was collected via *vena cava* from non-fasted animals in EDTA-
250 precoated tubes (BD Vacutainer K2E, 367864, BD) and centrifuged at 2000 g for 10 minutes. Plasma

251 was stored at -80°C until further use. Triglyceride levels were determined by the clinical chemistry
252 department (Centraal Diagnostisch Laboratorium, MUMC).

253 ## 8. Immunohistochemistry

254 Brains were sliced into free-floating sections of 30 µm thickness using a vibratome (Leica VT1200,
255 Leica Microsystems). For each immunofluorescent staining, two brain slices (Bregma +1.6 mm; Bregma
256 +2.2 mm) were included and two FOVs per section were imaged from deep cortical regions. Coronal
257 sections were stored in PBS with 0.1% sodium azide until staining. First, slices were washed with PBS
258 supplemented with 0.1% Triton-100 (PBS-T, Sigma-Aldrich, X100), PBS and PBS-T for 10 minutes and
259 blocked with 1% bovine serum albumin (BSA, VWR, 422361V) diluted in PBS-T for 1.5h at room
260 temperature. Briefly, sections were stained overnight (4°C) with anti-rat IgG-biotin (1:500 dilution in
261 PBS-T, Jackson ImmunoResearch, 712-065-150) to assess blood-brain barrier (BBB) permeability,
262 followed by incubation with streptavidin Alexa Fluor™ 594 conjugate (ThermoFisher, S11227) for 2h.
263 Following washing steps, cerebral vessels were stained using a tomato lectin (1:100 dilution in PBS-T,
264 Lycopersicon Esculentum (tomato) Lectin, DyLight 649, Vector Laboratories, DL-1178). Finally, sections
265 were mounted with antifading mounting medium (Invitrogen, P36980).

266 ### *Vascular density*

267 Image stacks (x=275 µm, y=275 µm, z=10 µm, 2 µm step size) of lectin-stained brain sections (n=4-
268 10/group) were acquired on a confocal microscope (Leica DMI 4000B, Leica Microsystems) at a 40x
269 magnification using Leica Application Suite Advanced Fluorescence (LAS AF) software (Leica
270 Microsystems). For each FOV, a maximal intensity projection was prepared in ImageJ (FIJI Distribution,
271 NIH). Vascular density, branching points and average vessel length were determined with Angiotool
272 (19). The following parameters were applied: vessel diameter: 3-8; intensity: 50-255; remove small
273 particles: 40. Images were excluded from the analysis when the signal-to-noise ratio was incompatible
274 with the Angiotool analysis. For each animal, images from two brain slices were averaged. The analysis
275 was performed by an experimenter blinded to the groups.

276 *BBB permeability*

277 To identify the presence of IgG leakages (n=8-10/group), brain sections were scanned using an
278 ImageXpress Pico Automated Live Cell Imager (Molecular Devices, San Jose, USA) at 10x magnification
279 (1 pixel = 0.69 µm). Acquired images were automatically stitched by the software (CellReporterXpress
280 software, Molecular Devices). BBB permeability was determined by the extravasation of IgG from
281 vessels into the parenchymal tissue. The number and size (surface area) of the leakages were assessed
282 in Arivis Vision 4D (version 3.6.2, Zeiss). In short, a machine learning segmentation was performed to
283 identify background (tissue negative for lectin and IgG signals), vessels (lectin-positive structures) and
284 IgG proteins (IgG-positive signal). A subtraction was performed to identify "IgG objects" outside the
285 "vessels objects" i.e. extravascular IgG signal. The obtained IgG leakages were then filtered to remove
286 artificial IgG background signal (objects <500 μm^2) and the number and size (surface area, μm^2) of IgG
287 leakages was exported for analysis.

288 9. Myelin integrity

289 A Luxol fast blue staining of brain sections from ZSF1 and Wistar rats was performed to estimate
290 white matter area and myelin content of the pericallosal white matter (defined as the corpus callosum
291 and adjacent lateral white-matter tracts, including the external capsule). The protocol was adapted
292 from Santiago et al. 2018 (20). Free-floating sections (Bregma +2.2 mm) were transferred to adhesive
293 glass slides to be air-dried overnight. After 24h incubation with Luxol fast blue (Solvent Blue38, Carl
294 Roth GmbH, 7709.3), differentiation of the white matter was completed using 0.1% lithium carbonate
295 (Merck, 105676). After washing steps with 70% ethanol (Boom B.V., 64-17-5) and demi water, sections
296 were incubated with cresyl violet (Carl Roth GmbH, 7651.2) followed by differentiation in 6% acetic
297 acid-ethanol (Acetic Acid, ThermoFisher, S25118A) for five minutes each. Finally, sections were
298 mounted with Entellan (Sigma-Aldrich, 1.07961) and imaged at 10x magnification using a BX50
299 microscope (Olympus) connected to a MBF camera (MBF Bioscience CX9000) and a MAC5000
300 Controller system (Ludl Electronic Products Ltd, 73 05020). Images were visualized and processed with

301 Stereo Investigator software (version 2020, MBF Bioscience, MicroBrightField). The Cavalieri method
302 was used to estimate the pericallosal white matter and whole brain area. The ratio of the pericallosal
303 white matter area over whole brain area was then used to assess white matter atrophy. Myelin content
304 was assessed using LFB mean gray value (MGV) intensities. LFB images were converted from ScanScope
305 Virtual Slide files to TIFF files using Qupath (Qupath-0.5.1., Belfast, Northern Ireland). An in-house built
306 ImageJ script was developed to perform background corrections. The background corrected LFB
307 images were processed using ImageJ. The ROIs covering the pericallosal white matter (corpus callosum
308 and external capsule) and the striatum were delineated using a custom ImageJ script. During this
309 analysis, LFB images were converted to a grayscale format, from which MGV data was extracted. To
310 increase interpretability, LFB values were inverted and converted into percentages. Decreased relative
311 LFB corresponds to decreased myelin content.

312 In addition, myelin integrity was assessed using polarized light imaging (PLI). PLI is a novel imaging
313 technique that leverages the birefringent properties of myelin sheaths to assess fiber orientation in
314 histological brain sections (21-24). By transmitting polarized light, this method enables quantitative
315 estimations of fiber orientation and inclination within a given sample (22). PLI has the potential to
316 identify early indicators of WM damage, surpassing the diagnostic sensitivity of traditional
317 histochemical techniques such as LFB staining (21). The sections were mounted onto glass microscope
318 slides and dried at 37 °C overnight. Subsequently, dried slides were coated with polyvinylpyrrolidone
319 (PVP; Sigma-Aldrich, 9003-39-8, Darmstadt, Germany) and covered with 24x60 mm coverslip glasses
320 in a laminar flow cabinet. To ensure optimal preservation, the prepared slides were left to dry under
321 controlled conditions for two weeks. The slides were then imaged using a PLI microscope (Zeiss
322 Axioplan microscope, Germany) equipped with a RGB-camera (Axiocam ERc 5s, Zeiss, Germany).
323 Background correction images were taken at the start of every imaging session to be utilized during
324 post-processing. Bregma +0.48 mm was selected from the atlas of the rat brain to be imaged for this
325 study. Two FOVs were acquired; each FOV was acquired in nine sequential images at rotation between
326 0 and 160 degrees. The raw images underwent post-processing in Matlab (MATLAB R2020b;

327 MathWorks Inc., Natick, MA, USA), wherein images were fitted to Jones Calculus. Background
328 corrections were performed and FOVs were stitched together for each of the nine sequential images
329 per rat brain, facilitating the construction of PLI maps; dispersion, FOM-HSV, inclination, in-plane,
330 retardance, and transmittance. The retardance (myelin density), dispersion (myelin quality), and
331 inclination maps were then imported into ImageJ to delineate the pericallosal white matter (corpus
332 callosum and external capsule) and the striatum as ROIs using a Wacom IntuosPro Small pen tablet
333 (Model PTH-451, Düsseldorf, Germany). MGV was recorded for dispersion and retardance for each ROI
334 per section. For retardance, the higher the MGV, the better the myelin density. In standard
335 interpretation, lower MGV scores for dispersion are indicative of better myelin quality. However, to
336 enhance interpretability, dispersion values were inverted and both the inverted dispersion data and
337 the untouched retardance MGV values were converted into percentages. Within this framework,
338 higher relative dispersion and retardance values correspond to improved myelin quality and density.

339 ## 10. Gene expression analysis of brain microvessels

340 ### *Isolation of brain microvessels*

341 Cortical brain microvessels were freshly isolated from one cerebral hemisphere immediately after
342 sacrifice. The cortex was homogenised in cold, sterile PBS using a tissue grinder and centrifuged for
343 five minutes at 2000 g. The resulting pellet was then suspended in 15% dextran-PBS (Sigma Aldrich,
344 31390) and centrifuged at 4300 g for 15 minutes. After dissolving the pellet in PBS containing 1% BSA
345 (Fatty Acid-free, Sigma Aldrich, 126609), the solution was transferred to a 100 µm cell strainer
346 (Pluriselect, 43-57100-51), followed by filtration through a 20 µm nylon mesh (Pluriselect, 43-50020-
347 03). Brain microvessels remaining on the latter filter were collected using 0.5% BSA-PBS (Fatty Acid-
348 free, Sigma Aldrich, 126609) and centrifuged at 4300 g for 10 minutes. The final pellet was either
349 suspended in DPBS and air-dried for immunohistochemistry, or TRIzol (ThermoFisher Scientific,
350 15596018) for RNA isolation, and stored at -80°C.

351 ### *Characterization of brain microvessels*

352 Microvessels were washed and permeabilized with 0.1% IGEPAL (Sigma Aldrich, CA-630) in TRIS-
353 buffered saline (TBS), TBS and 0.1% IGEPAL-TBS for 5 minutes. Unspecific binding was blocked with 3%
354 donkey serum in TBS for 1h. Briefly, primary antibodies were diluted in 0.1% IGEPAL-TBS supplemented
355 with 0.3% donkey serum and incubated overnight (4°C): goat anti-pericyte-derived growth factor
356 receptor β (PDGFR-β, 1:100, R&D systems) and rabbit anti-ionized calcium-binding adapter molecule
357 1 (Iba-1, 1:500, FUJIFILM Wako Chemicals, 019-19741). Following washing steps, samples were
358 incubated for 1h at room temperature with corresponding secondary antibodies dissolved in 0.1%
359 IGEPAL-TBS supplemented with 0.3% donkey serum: donkey anti-goat AF488 (1:200, Invitrogen, A-
360 21202) and donkey anti-rabbit AF488 (1:500). To detect astrocytic endfeet, samples were first blocked
361 with 1% BSA + 3% donkey serum in 0.1% IGEPAL-TBS, followed by overnight incubation with rabbit
362 anti-aquaporin 4 (1:1000, Sigma, A5971) and visualized with donkey anti-rabbit AF488 (1:500) diluted
363 in 0.1% IGEPAL-TBS containing 1% BSA. Following washing steps, cerebral microvessels were stained
364 overnight with tomato lectin diluted in 0.1% IGEPAL-TBS supplemented with 0.3% donkey serum at
365 4°C. Counterstaining of the nuclei was performed using NucBlue (Invitrogen, R37606) according to the
366 manufacturer's instructions. Finally, slides were mounted using antifading mounting medium.

367 *RNA isolation, library preparation and bulk RNA sequencing*

368 For samples of the first time point, microvessels from two rats (8-9w) were pooled into one sample
369 before RNA isolation because of the young age of the animals. RNA was extracted from brain
370 microvessels of Lean and Obese ZSF1 rats using TRIzol according to the manufacturer's protocol and
371 stored at -80°C until further processing. RNA purity and integrity (RIN) were checked according to the
372 manufacturer's protocol using Nanodrop One (ThermoFisher Scientific) and Agilent 2100 Bioanalyzer
373 system (Agilent Technologies) respectively. Purification of the mRNA (n=4/group/time point) and
374 library preparation were performed according to the manufacturer's protocol using the RiboNaut™
375 rRNA Depletion Kit (NETFLEX, NOVA-512963, PerkinElmer) and the Rapid Directional RNA-Seq Kit 2.0
376 (NETFLEX, NOVA-5198, PerkinElmer), respectively. Lastly, sequencing was performed on an S1 flow cell
377 using the Novaseq 6000 sequencing system (NovaSeq 6000, Illumina, Inc).

378 *Transcriptomic analysis*

379 Raw sequencing data was trimmed using fastp (25). The R package 'DESeq2' was used to identify
380 DEGs using a p-value (false discovery rate; FDR) below 0.05 and a fold change above 1.5 (26, 27). Gene
381 Ontology enrichment analysis was performed to identify overrepresented biological processes in the
382 list of DEGs using the clusterProfiler R-package (v. 4.12.6, (28). Protein-protein interaction networks of
383 selected GO terms were created using the stringApp (v. 2.1.1, (29)) and visualized in Cytoscape
384 (v3.10.1) (30) using the RCy3 R-package (v. 2.24.0, (31)).

385 ## 11. RNAscope assay

386 RNAscope™ Multiplex Fluorescent Detection kit v2 (Advanced Cell Diagnostics, ACD, Bio-Techne
387 Gmbh, 323120) was performed according to the manufacturer's instructions. Specific mRNA probes
388 were designed against rat *Klf2* (111711-C1) and *Trpv4* (476661-C2) targets. Three-plex positive and
389 negative control probe mixtures were included in the experiment (**Figure S10**). All baking steps were
390 performed in the ACD Hybez II Hybridization Oven (ACD, 321710).

391 The multiplex detection of mRNAs was performed on paraffin-embedded ZSF1 brains of Lean and
392 Obese animals at 22-23 and 34-35 weeks of age. After incubating the sections with protease for 30
393 min, the solution was replaced with fresh protease PLUS for another 10-min incubation. Following
394 probe hybridization, brain sections were stored overnight in saline sodium citrate buffer. TSA Vivid
395 Fluorophores 570 (channel C1, 323272, 1:1500) and 650 (channel C2, 323273, 1:1500) were used to
396 visualize *Klf2* and *Trpv4* probes, respectively. Lycopersicon Esculentum Lectin (DyLight 488, Vector
397 Laboratories, DL-1174-1) was used to detect blood vessels following RNAscope procedure.

398 Slides were imaged (x=175 µm, y=175 µm, z= 6 µm, 0.5 µm step size) with confocal microscopy at
399 a 63x magnification (Leica SPE, Leica Microsystems B.V. Amsterdam). For each rat brain (n=4/group),
400 three FOVs were acquired and analyzed in Arivis Vision 4D (version 3.6.2, Zeiss, Rostock, Germany).
401 Machine learning segmentation was performed to identify background, lectin-positive signal, and *Klf2*
402 and *Trpv4* transcripts. Next, the compartments feature was applied to identify only *Klf2* and *Trpv4*

403 signal inside the vessel objects. From this procedure, several parameters about the target expression
404 in the vascular network were extracted: number of transcripts and total intensity. All parameters were
405 corrected for the total vessel volume.

406 ## 12. Statistical analyses

407 Group size was calculated a priori for both animal studies (see above description of Study 1 and
408 Study 2) using G*Power3.1. For study 1, the discrimination index d2 has been chosen as primary
409 outcome parameter for group size calculation due to its high variability compared to other cognitive
410 readout parameters: ANOVA with repeated measures, effect size f=0.25, α error = 0.05; power β =
411 0.80, and considering a possible 15% drop-out rate, resulting in n=15 animals/group. For study 2, the
412 change in CBF has been chosen as primary outcome parameter for group size calculation as it was
413 central to answer our research question: ANOVA, effect size f=0.90, α error = 0.05; power β = 0.80,
414 and considering a possible 5% drop-out rate, resulting in min n=11 animals/group for the primary
415 readout parameter. Considering required sample sizes for post-mortem analyses and to be consistent
416 with the group size in Study 1, the group size in Study 2 was increased to n=14 animals/group.

417 Data are represented as mean ± SEM. All statistical analyses were performed with GraphPad Prism
418 10.0.1 software (San Diego, USA). Normality distribution was tested with the Shapiro-Wilk test. Two-
419 way analysis of variance (ANOVA) was used to compare Lean and Obese groups over time, followed by
420 Sidak's post hoc testing with correction for multiple comparisons. One-sample t-tests were performed
421 to determine whether: the alternation percentage in ZSF1 rats was different from 50% during the YM;
422 the discrimination index d2 was significantly different from 0 during the NORT; and whether cerebral
423 blood flow, neurovascular coupling, vascular density, the number of branching points, white matter
424 content, and BBB integrity of ZSF1 rats differed from Wistar rats. *P*-values <0.05 were considered
425 statistically significant.

426

427 # RESULTS

428 In this study, we used male Zucker fatty and spontaneously hypertensive (ZSF1) rats as a model for
429 HFpEF and comorbidities. For cardiovascular and cognitive characterisation, only Lean and Obese ZSF1
430 animals were studied, while Wistar rats were included as a normotensive reference group for the *in*
431 *vivo* assessment of microvascular function and post-mortem IHC analyses.

432 ## 1. Cardiovascular phenotype: Obese ZSF1 rats develop HFpEF

433 Systolic and diastolic blood pressures were increased in all ZSF1 rats at each time point compared
434 to normotensive values reported in a previous publication (dashed line; single t-test: $p_{systolic}<0.0001$,
435 **Figure 1A**; $p_{diastolic}<0.01$, **Figure S1A**) (32). Moreover, Obese ZSF1 rats showed a significantly higher
436 blood pressure at 20w compared to Lean animals ($p_{systolic}<0.01$, $p_{diastolic}<0.01$). The development of
437 obesity and diabetes was monitored over time; an increase in body weight ($p<0.0001$, **Figure S1B**) and
438 FBG ($p<0.05$, **Figure 1B**) was observed in Obese rats starting from 5 and 10 weeks of age, respectively.
439 In addition, triglyceride levels were elevated in Obese vs Lean at 22-23w and 34-35w ($p<0.0001$, **Figure**
440 **1C**).

441 The progression of HFpEF in ZSF1 rats was assessed at the age of 7, 21, and 31 weeks using
442 echocardiography. All animals showed a preserved ejection fraction (EF) above 50%, moreover, Obese
443 ZSF1 rats had a significantly higher EF at all disease stages compared to Lean animals ($p_{7w}<0.001$,
444 $p_{21w}<0.01$, $p_{31w}<0.0001$, **Figure S2**). Pulse wave Doppler measurements of the mitral valve indicated a
445 decrease in the ratio of rapid filling (early mitral inflow peak velocity, E) over atrial contraction (late
446 mitral inflow peak velocity, A) in Obese animals at 21 and 31w ($p<0.0001$, **Figure 2A**). The isovolumetric
447 relaxation time (IVRT) was significantly higher in Obese vs Lean at 21w and a tendency towards
448 increased IVRT was observed at 31w ($p_{21w}<0.05$, $p_{31w}=0.10$ **Figure 2B**). This was accompanied by an
449 elevated deceleration time in Obese ZSF1 rats at 21w ($p<0.001$, **Figure 2C**).

450 Moreover, the measurement of pulmonary peak velocities (p_{7w}<0.01, p_{21w}<0.0001, **Figure 2D**) and
451 aorta peak velocities (p_{7w}<0.001, p_{21w}<0.0001, **Figure 2E**) showed a significant increase in Obese vs
452 Lean at the first two time points, while being decreased at 31w (p<0.0001). During diastole, anterior
453 LV wall was thickened in Obese ZSF1 rats at 21w (p<0.001) and 31w (p<0.05). Other echocardiographic
454 parameters are available in **Figure S2** and **Figure S3**. Altogether, the assessment of cardiac function
455 confirmed HFpEF pathology in Obese ZSF1 rats at both 21w and 31w, and was furthermore associated
456 with an elevated heart weight/tibia length ratio at each disease stage (**Figure S4**).

457 ## 2. Cognitive function: impaired performance in Obese ZSF1 rats

458 A series of behavioural testing was performed to assess anxiety, working memory, short-term
459 memory, and long-term spatial learning/memory using the elevated zero maze (EZM), Y-maze, novel
460 object recognition task (NORT), Barnes maze (BM), respectively (**Figure 3A-D**). Obese ZSF1 rats were
461 more anxious at 30-32 weeks old, spending less time in the open arms compared to Lean rats in the
462 EZM (p<0.001, **Figure 3E**). Lean animals became less anxious over time ($p_{20\text{-}22w}$<0.05 and $p_{30\text{-}32w}$<0.01
463 vs 14-16w), whereas the number of open arm entries remained unchanged between groups (**Figure**
464 **S5A**). During the YM task, working memory was not affected by comorbidities at any of the time points,
465 only Lean rats showed an impaired working memory at 30-32w (single t-test: p<0.05 vs t=50 (33),
466 **Figure 3F**). When comparing Obese rats of 30-32w to 14-16w, a significant decrease in working
467 memory was observed. In addition, the percentage of alternations (p_{age}<0.001) decreased over time,
468 while the relative time spent in centre remained unchanged (**Figure S5C-D**). Lastly, locomotor activity
469 in both the EZM and YM task was lower in Obese ZSF1 rats at 14-16w (**Figure S5B**). Although impaired
470 working memory could not be confirmed in the Obese, Lean rats did have a significant impairment of
471 working memory at the latest time point. This could be due to a decrease in the number of entries over
472 time (p_{age}<0.0001), especially in Obese animals at 20w and 30w of age. In addition, Obese rats were
473 slightly more anxious than the Lean, which might have affected their capability to alternate as well
474 during the YM task.

475 Two-way ANOVA revealed short-term memory impairment in Obese ZSF1 rats at 30-32 weeks of
476 age (single t-test: $p<0.05$ vs d2=0) during the novel object NORT, and at this time point, the
477 discrimination index d2 was significantly lower in Obese vs Lean (**Figure 3M**). Furthermore, total
478 exploration time during this task was not different between groups (**Figure S5E**). Spatial learning was
479 assessed in the BM task and was found to be impaired in Obese vs Lean starting from 20-22w (**Figure**
480 **3H-J**). In the 30-seconds probe trial, a significant decrease in long-term spatial memory was observed
481 in Obese animals compared to Lean rats ($p_{group}<0.05$, **Figure 3K**), and reversal learning was affected by
482 aging ($p_{age}<0.0001$, $p_{age\ x\ group}<0.01$, **Figure 3L**). During this task, locomotor activity was significantly
483 lower in Obese ZSF1 rats at all time points (**Figure S5F**).

484 ## 3. Brain atrophy and early white matter deficits in Obese ZSF1 rats

485 Brain atrophy was observed in Obese vs Lean ZSF1 rats at 8-9w ($p<0.0001$) and 22-23w ($p<0.0001$,
486 **Figure 4B**). Within Lean and Obese groups, brain size also decreased significantly over time ($p<0.0001$).
487 The relative proportion of white matter area was also lower in Obese animals at 22-23w and 34-35w
488 compared to Lean ($p<0.05$, **Figure 4C**). Moreover, within the Lean and Obese group, the relative size
489 of the pericallosal area was significantly higher over time, due to the progression of brain atrophy.
490 Myelin content, as measured by the relative LFB signal, was decreased in Obese vs Lean animals in
491 both the pericallosal and striatum areas (pericallosum $p_{group}=0.04$, **Figure 4D**; striatum $p_{group}=0.02$,
492 **Figure 4E**). The relative retardance, corresponding to myelin density, increased over time
493 independently of the groups in both areas (pericallosum $p_{group}<0.0001$, **Figure 4F**; striatum $p_{group}<0.001$,
494 **Figure 4G**). The relative dispersion, corresponding to myelin quality, was not affected by age in the
495 pericallosal area but increased in the striatum area ($p_{age}<0.0001$, **Figure 4I**). There was only a mild
496 decrease observed between Obese and Lean groups in the striatum ($p_{group}=0,051$, **Figure 4I**).

497 ## 4. Impaired neurovascular coupling in Obese ZSF1 rats

498 Cerebral blood flow was measured over the barrel cortex using laser speckle contrast imaging (LSCI)
499 (**Figure 5A-C**). Baseline cortical cerebral blood flow and neurovascular coupling were assessed in ZSF1

500 rats at three different time points and in Wistar rats at 20-21w as a normotensive reference. Although
501 baseline cerebral blood flow remained unchanged between Lean and Obese groups across all ages
502 (**Figure 5D**), all ZSF1 animals had a significantly lower cerebral blood flow compared to Wistars at all
503 time points (single t-test: $p<0.05$ vs Wistars). Moreover, blood flow declined significantly over time
504 ($p_{age}=0.02$), and a trend towards decreased baseline cerebral blood flow was observed in Obese rats at
505 32-33w vs 6-7w ($p=0.0519$) (**Figure 5D**). Neurovascular coupling, presented as the percentage increase
506 in cerebral blood flow during whisker stimulation, was significantly decreased in Obese vs Lean at the
507 second ($p<0.001$) and third ($p<0.05$) time point (**Figure 5E**). The impaired neurovascular coupling at 33
508 weeks of age was replicated in a separate study (**Figure S6**). In addition, cerebral blood flow increase
509 to stimulation was significantly lower in ZSF1 rats at 6-7w, and in Obese animals at 20-21w and 32-33w
510 compared to Wistar rats (single t-test: $p<0.05$ vs Wistars). Within Lean and Obese groups, the response
511 to whisker stimulation was smaller at the first time point compared to 20-21w and 32-33w ($p<0.01$),
512 which could be explained by an immature neurovascular coupling at 6-7w.

513 5. Obese ZSF1 rats showed increased cerebral vascular density and BBB leakage size

514 The microvascular network was assessed in the brain of ZSF1 rats at three different time points
515 and in Wistar rats (22-23w). In addition to the group and interaction effect ($p_{group}=0.02$, $p_{age\ x\ group}=0.03$,
516 **Figure 6A-E**), cortical vascular density was found to be higher in Obese vs Lean only at 34-35w ($p<0.01$).
517 At this age, vascular density in the cortex was also significantly elevated compared to Wistar rats (single
518 t-test: $p<0.05$ vs Wistars) and Obese rats at 22-23w ($p<0.01$). Although the density of branching points
519 was similar between Lean and Obese groups, it was lower than in Wistar rats at 8-9w and 22-23w
520 (single t-test: $p<0.05$ vs 349 ± 63 junctions/mm^2, **Figure 6F**). In addition, the size of BBB leakages in the
521 whole brain increased over time and was higher in the Obese group ($p_{age}=0.0026$, $p_{group}=0.02$). Whereas
522 the number of BBB leakages **(Figure 6G-J**) per brain section was not different between Lean and Obese
523 groups at any time point, the leakage size was significantly higher in Obese vs Lean at 22-23w ($p<0.01$).
524 At this age, the size of BBB leakages within the Obese group was also higher than at 8-9w.

525 ## 6. Transcriptomic analysis of cortical microvessels

526 Isolated microvessels from the brain cortex of ZSF1 rats were characterized by immunofluorescent
527 staining against markers for pericytes (PDGFR-β), microglia (Iba-1), astrocytic endfeet (aquaporin 4),
528 and endothelial cells (tomato-lectin) (**Figure S7A-C**). Confocal imaging confirmed the presence of
529 pericytes and astrocyte endfeet around the isolated cortical microvessels, whereas microglia could not
530 be detected in the samples. The average diameter of the isolated vessels was 5.7 ± 1.2 µm (**Figure**
531 **S7D**). Transcriptomic data revealed a total of 98, 254 and 487 differentially expressed genes (DEGs) in
532 Obese vs Lean at 8-9w, 22-23w and 34-35w, respectively ($p<0.05$, absolute fold change>1.5; **Figure 7A-**
533 **C**). Following Gene Ontology analysis, an overview of the main enriched biological processes was
534 generated at each time point and further clustered into functional categories (22-23w in **Figure 7D**; 8-
535 9w and 34-35w in **Figure S 8** and **Figure S9**). This analysis revealed a high regulation of processes
536 related to angiogenesis and immune mechanisms in Obese vs Lean at the first time point. By 22-23w,
537 these processes were still enriched, in addition to blood vessel formation and vasoreactivity. At the
538 final time point, processes associated with blood vessel formation, vasoreactivity and vessel
539 remodelling were significantly regulated.

540 Within these biological processes, Transient Receptor Potential Vanilloid 4 (*Trpv4*) and Krüppel-
541 Like Factor 2 (*Klf2*), two genes that are involved in many of the enriched processes, were highly
542 downregulated at both the second (p_{Klf2}=0.00007, $\log2FC_{Klf2}$=-1.33; p_{Trpv4}=0.02, log2FC=-1.18) and third
543 (p_{Klf2}=0.0004, $\log2FC_{Klf2}$=-1.04; p_{Trpv4}=0.04, $\log2FC_{Trpv4}$=-1.21) time point in Obese vs Lean. Moreover,
544 they were specifically regulated within the Obese groups but not in the Lean groups over time. Both
545 genes are involved in processes related to 'regulation of tube diameter' (p_{adj}=0.02), 'blood vessel
546 diameter maintenance' (p_{adj}=0.02), 'regulation of tube size' (p_{adj}=0.02), and 'vascular process in
547 circulatory system' (p_{adj}=0.03) at the second time point, and the process 'vasodilation' (p_{adj}=0.003) at
548 the last time point. The protein-protein interaction network of all proteins associated with the
549 overarching GO term GO:0003018 'vascular process in circulatory system' is represented in **Figure 7E**.
550 The DEGs within this process include Requirement A Serine Peptidase 1 (Htra1), Klf2, Trpv4,

551 Angiotensin-Converting Enzym (Ace), Matrix Metallopeptidase 2 (Mmp2,) 5-Hydroxytryptamine
552 (Serotonin) Receptor 2C (Htr2c), Superoxide Dismutase 3 (Sod3), and Plasmalemma Vesicle Associated
553 Protein (Pvlap), and their expression profile at 22-23w and 34-35w is represented in a heatmap in
554 **Figure 7F**, with on average a lower expression level in Obese vs Lean, except Htra1 which is
555 upregulated. Among these DEGs, *Trpv4* and *Klf2* are interacting with 32 and 17 other proteins, making
556 them very central in this GO term.

557 ## 7. Multiplex detection of *Klf2* and *Trpv4* expression in ZSF1 brains

558 In order to validate the downregulation of *Klf2* and *Trpv4* identified from cortical microvessels at
559 22-23w and 34-35w, a multiplex RNAscope was performed on paraffin-embedded brains from the
560 same Lean and Obese animals used for the RNA sequencing (**Figure 8A-D, Figure S10**). The number of
561 transcripts and total intensity of *Klf2* expression (**Figure 8E-F**) was significantly decreased in Obese vs
562 Lean at 22-23w ($p<0.001$). The number of *Trpv4* transcripts was decreased ($p<0.05$) with a trend
563 towards a lower signal intensity ($p=0.06$) in the Obese animals at this timepoint (**Figure 8G-H**). At the
564 age of 34-35w, however, no significant differences were observed in the number or intensity of *Klf2*
565 and *Trpv4* transcripts. In addition, two-way ANOVA indicates a group and interaction effect for both
566 the number ($p_{group}=0.01$, $p_{age\ x\ group}=0.0009$) and intensity ($p_{group}=0.01$, $p_{age\ x\ group}=0.0005$) of *Klf2*
567 transcripts, whereas only the interaction effect is observed in the number ($p_{age\ x\ group}=0.02$) and
568 intensity of *Trpv4* signal ($p_{group\ x\ age}=0.04$). In summary, the downregulation of both targets could be
569 confirmed at the second, but not at the third timepoint.

570

571 # DISCUSSION

572 Alongside confirming the development of the comorbidities and HFpEF in this model, we
573 demonstrated progressive cognitive impairment in Obese rats starting from 20 weeks of age. Obese
574 animals had short-term memory impairment, altered spatial learning, and impaired long-term
575 memory, while working memory and reversal learning remained similar to Lean rats. As expected, mild
576 cognitive decline was also observed in Lean hypertensive animals at the final time point, as suggested
577 by the impaired working memory and the smaller difference in performance between Lean and Obese
578 during the Barnes Maze task. The overall cognitive dysfunction was furthermore associated with brain
579 atrophy and decreased myelin content in Obese ZSF1 rats.

580 In addition to cognitive decline, the longitudinal study of ZSF1 rats provided more insight into the
581 chronic impact of comorbidities on cerebrovascular reactivity. Endothelial dysfunction has been
582 recognized as an important hallmark of cSVD, as confirmed in a systematic review and meta-analysis
583 of 29 studies, who reported a reduced neurovascular coupling in different forms of cSVD (34). Our
584 findings indicated that impaired neurovascular coupling is present in Obese ZSF1 rats starting from 22-
585 23w, and this was associated with the development of cognitive impairment. The response to whisker
586 stimulation was also found to be lower at 6-7w in both ZSF1 groups compared to later time points and
587 Wistars, possibly due to an immature vascular reactivity at this age (35, 36). Although no significant
588 difference in baseline cerebral blood flow was detected at any time point, it did decrease over time.
589 Given the limited imaging depth of LSCI, it is also possible that perfusion in deeper regions of the brain
590 is affected to a greater extent.

591 Together with the development of cognitive impairment and neurovascular dysfunction, Obese
592 ZSF1 rats exhibited brain atrophy, a common feature in cSVD. By applying a multimodal assessment of
593 white matter area, myelin content, density, and integrity, we were able to detect mild, yet meaningful
594 microstructural defects in Obese ZSF1 rats. In addition to reduced brain volume, Obese animals

595 showed subtle but consistent reductions in white matter area, in myelin content and early signs of
596 compromised myelin quality within the striatum. Age-related increases in myelin density were evident
597 in both Lean and Obese groups, likely reflecting ongoing maturation at this stage(36-38). Altogether,
598 these data support the concept that comorbid metabolic stress and neurovascular uncoupling begin
599 to drive structural white matter vulnerability early in the disease course.

600 Considering the cognitive, neurovascular, and white-matter deficits identified in this model, we
601 next assessed whether comorbidities extend their impact to the structure and permeability of the
602 cerebral microvasculature. Immunohistochemical analysis showed an increase in both BBB leakage size
603 and microvessel density at the second and third time point, respectively. Some controversy exists on
604 the vascular density in cSVD; various papers have reported decreased vascular density while others
605 observed an increase, similar to our findings. It is well established that high blood pressure, one of the
606 risk factors for cSVD, is associated with capillary rarefaction, as observed by Suzuki et al. in renal
607 hypertensive rats (39). On the other hand, Liu et al. confirmed enhanced neovascularization as well as
608 microvascular hypoperfusion in adult leptin-receptor deficient mice (40). In addition, vascular density
609 and permeability were elevated in obese mice fed with a high-fat diet (41). Our data suggest that,
610 despite the increased number of microvessels, these new vessels are more unstable and dysfunctional,
611 and therefore unable to properly respond to the needs of the brain's parenchyma. We propose that
612 the observed enhanced vascularization at the latest time point serves as a compensatory mechanism
613 for the chronic hypoperfusion and impaired cerebrovascular reactivity in Obese ZSF1 rats. The resulting
614 increase in permeability may further initiate or exacerbate an inflammatory cascade.

615 Our study aimed at examining the molecular processes central to the development of VCI in this
616 HFpEF model by studying the transcriptomic regulations within cortical brain microvessels at three
617 different time points. The Gene Ontology analysis revealed a clear evolution of regulated processes
618 over time. At the first time point, many processes were related to immune mechanisms, which were
619 still detected at the second time point. Subsequently, processes related to angiogenesis and

620 vasodilation became highly enriched, highlighting the functional changes in the vasculature. By 34-
621 35w, the enrichment of processes linked to angiogenesis, vasoreactivity, and vessel remodelling
622 emphasize ongoing structural changes. These data align with the observed impaired neurovascular
623 coupling starting at 22-23w, as well as the increased vessel density at the final stage.

624 We further validated *Trpv4* and *Klf2* as important targets in processes related to vascular reactivity.
625 Notably, *Trpv4* and *Klf2* downregulation were specific to the Obese group; a decrease in expression
626 was observed at both the second and third time point, while this reduced expression was not detected
627 in Lean rats. The Ca^{2+}-permeable TRPV4 channel is known to play a crucial role in regulating vascular
628 tone, angiogenesis, BBB integrity, and neuro-inflammation (42-44). A decline in NO production was
629 observed when *Trpv4* was downregulated, resulting in impaired vasodilation (43). In addition, TRPV4-
630 mediated dilation has been associated with cognitive function and cerebrovascular reactivity (45, 46).
631 Secondly, *Klf2* is involved in anti-inflammatory, anti-angiogenic and anti-oxidant activities, and is
632 known to trigger eNOS expression in endothelial cells, thereby inducing vasodilatory effects (47).
633 Reduced expression of *Klf2* was found in the brain of Alzheimer patients, and upregulation of
634 endothelial *Klf2* has been shown to attenuate Aβ-induced cytotoxicity and improve mitochondrial
635 function (48). We were able to validate the downregulation of *Trpv4* and *Klf2* at 22-23w but not at 34-
636 35w. This discrepancy might be explained by the difference in the material used between the two
637 approaches (isolated microvessels vs endothelial cells). Since the transcriptomic analysis was
638 performed on bulk RNA extracts from brain microvessels, comprising endothelial cells, pericytes and
639 astrocyte endfeet, we cannot elaborate on the respective cell type contribution. Nevertheless, it is well
640 described that *Trpv4* and *Klf2* have a more prominent function in endothelial cells (49, 50).

641 Beyond the diagnostic challenges, current treatment strategies primarily focus on slowing the
642 progression of comorbidities (e.g. hypertension, type II diabetes), but no specific targeted therapy
643 exists for HFpEF nor VCI. Taken together, our results indicate for the first time that VCI is present during
644 HFpEF in ZSF1 rats. The presence of comorbidities and spontaneous development of both cardiac and

645 cerebral pathologies make this model unique and highly translational to investigate mechanisms
646 underlying cSVD. This study demonstrates the downregulation of *Trpv4* and *Klf2,* which was associated
647 with the onset of neurovascular uncoupling, as well as increased BBB permeability and vascular
648 density. Given their mechanosensitive and vasoprotective properties, *Trpv4* and *Klf2* could be
649 promising therapeutic targets for cerebrovascular dysfunction. Although two clinical trials reported
650 the safety of the TRPV4 antagonist GSK2798745 in healthy volunteers and patients with heart failure,
651 no clinical trials have investigated the use of TRPV4 agonists/antagonists in the context of neurological
652 dysfunction (51, 52). Due to the lack of specific treatments for cSVD and VCI, we suggest to further
653 explore the potential of these targets in other preclinical models, human tissue and clinical trials.

654

Declarations

Ethics approval and consent to participate: All experiments and procedures within this study were conducted in accordance with institutional guidelines and approved by the Ethical Committees for Animal Experiments of Maastricht University (AVD10700202010326).

Data availability of data and materials: Data are available upon reasonable request.

Competing interests: The authors declare no competing interests.

Funding: This research was supported by the European Union's Horizon 2020 project 'CRUCIAL' (grant number 848109) and by Horizon 2020 research and innovation programme under the Marie Skłodowska-Curie (grant agreement No 954798).

Authors' contributions: Conceptualization and study design: S.L., S.F.; Acquisition of research funding: S.F., E.J., R.v.O.; Performed in vivo and ex vivo experiments and data analysis: S.L.,L.v.T., I.P., P.L., N.B., D.M., D.H., S.S., E.W., H.S., F.A., M.W.; Performed the RNA sequencing study: M.v.H., R.K.; Performed and supported bioinformatic analyses: S.L., S.F., F.C., M.K.; Supervision and guidance: S.F., M.W., A.J.K., E.J., R.v.O.; All the authors contributed to the writing and reviewing of the paper and approved the final version.

Acknowledgements: Alessandra Pasut and Mieke Dewerchin, Laboratory of Angiogenesis and Vascular Metabolism, Department of Oncology and Leuven Cancer Institute (LKI), KU Leuven, VIB Center for Cancer Biology, VIB, Leuven, Belgium. All partners from the Horizon 2020 project 'CRUCIAL'.

REFERENCES

1. Dichgans M, Leys D. Vascular Cognitive Impairment. Circ Res. 2017;120(3):573-91.
2. Evans LE, Taylor JL, Smith CJ, Pritchard HAT, Greenstein AS, Allan SM. Cardiovascular comorbidities, inflammation, and cerebral small vessel disease. Cardiovasc Res. 2021;117(13):2575-88.
3. Papadopoulos A, Palaiopanos K, Protogerou AP, Paraskevas GP, Tsivgoulis G, Georgakis MK. Left Ventricular Hypertrophy and Cerebral Small Vessel Disease: A Systematic Review and Meta-Analysis. J Stroke. 2020;22(2):206-24.
4. Cermakova P, Lund LH, Fereshtehnejad SM, Johnell K, Winblad B, Dahlström U, et al. Heart failure and dementia: survival in relation to types of heart failure and different dementia disorders. Eur J Heart Fail. 2015;17(6):612-9.
5. Hillier E, Covone J, Fischer K, Chen HY, Hafyane T, Friedrich MG. Microvascular Dysfunction as a Possible Link Between Heart Failure and Cognitive Dysfunction. Circ Heart Fail. 2023:e010117.
6. Rundek T, Tolea M, Ariko T, Fagerli EA, Camargo CJ. Vascular Cognitive Impairment (VCI). Neurotherapeutics. 2022;19(1):68-88.
7. Tini G, Cannatà A, Canepa M, Masci PG, Pardini M, Giacca M, et al. Is heart failure with preserved ejection fraction a 'dementia' of the heart? Heart Fail Rev. 2022;27(2):587-94.
8. Alwerdt J, Edwards JD, Athilingam P, O'Connor ML, Valdés EG. Longitudinal differences in cognitive functioning among older adults with and without heart failure. J Aging Health. 2013;25(8):1358-77.
9. Simmonds SJ, Cuijpers I, Heymans S, Jones EAV. Cellular and Molecular Differences between HFpEF and HFrEF: A Step Ahead in an Improved Pathological Understanding. Cells. 2020;9(1):242.
10. Emfietzoglou M, Terentes-Printzios D, Kotronias RA, Marin F, Montalto C, De Maria GL, et al. The spectrum and systemic associations of microvascular dysfunction in the heart and other organs. Nat Cardiovasc Res. 2022;1(4):298-311.
11. Cuijpers I, Simmonds SJ, van Bilsen M, Czarnowska E, González Miqueo A, Heymans S, et al. Microvascular and lymphatic dysfunction in HFpEF and its associated comorbidities. Basic Res Cardiol. 2020;115(4):39.
12. Wong SM, Jansen JFA, Zhang CE, Hoff EI, Staals J, van Oostenbrugge RJ, et al. Blood-brain barrier impairment and hypoperfusion are linked in cerebral small vessel disease. Neurology. 2019;92(15):e1669-e77.
13. Brown LS, Foster CG, Courtney JM, King NE, Howells DW, Sutherland BA. Pericytes and Neurovascular Function in the Healthy and Diseased Brain. Front Cell Neurosci. 2019;13:282.
14. Deichl A, Wachter R, Edelmann F. Comorbidities in heart failure with preserved ejection fraction. Herz. 2022;47(4):301-7.
15. Schauer A, Draskowski R, Jannasch A, Kirchhoff V, Goto K, Männel A, et al. ZSF1 rat as animal model for HFpEF: Development of reduced diastolic function and skeletal muscle dysfunction. ESC Heart Failure. 2020;7(7):2123-34.
16. Cuijpers I, Carai P, Mendes-Ferreira P, Simmonds SJ, Mulder P, Miranda-Silva D, et al. The effect of different anaesthetics on echocardiographic evaluation of diastolic dysfunction in a heart failure with preserved ejection fraction model. Sci Rep. 2020;10(1):15701.
17. van Goethem NP, Rutten K, van der Staay FJ, Jans LA, Akkerman S, Steinbusch HW, et al. Object recognition testing: rodent species, strains, housing conditions, and estrous cycle. Behav Brain Res. 2012;232(2):323-34.
18. Koopmans G, Blokland A, van Nieuwenhuijzen P, Prickaerts J. Assessment of spatial learning abilities of mice in a new circular maze. Physiol Behav. 2003;79(4-5):683-93.
19. Zudaire E, Gambardella L, Kurcz C, Vermeren S. A computational tool for quantitative analysis of vascular networks. PLoS One. 2011;6(11):e27385.

20. Santiago A, Soares LM, Schepers M, Milani H, Vanmierlo T, Prickaerts J, et al. Roflumilast promotes memory recovery and attenuates white matter injury in aged rats subjected to chronic cerebral hypoperfusion. Neuropharmacology. 2018;138:360-70.
21. Sole-Guardia G, Luijten M, Janssen E, Visch R, Geenen B, Kusters B, et al. Deep learning-based segmentation in MRI-(immuno)histological examination of myelin and axonal damage in normal-appearing white matter and white matter hyperintensities. Brain Pathol. 2025;35(2):e13301.
22. Larsen L, Griffin LD, Grassel D, Witte OW, Axer H. Polarized light imaging of white matter architecture. Microsc Res Tech. 2007;70(10):851-63.
23. Lohkamp KJ, Kiliaan AJ, Shenk J, Verweij V, Wiesmann M. The Impact of Voluntary Exercise on Stroke Recovery. Front Neurosci. 2021;15:695138.
24. Lohkamp KJ, Timmer N, Sole Guardia G, Shenk J, Verweij V, Geenen B, et al. Sex-Specific Adaptations in Alzheimer's Disease and Ischemic Stroke: A Longitudinal Study in Male and Female APP(swe)/PS1(dE9) Mice. Life (Basel). 2025;15(3).
25. Chen S, Zhou Y, Chen Y, Gu J. fastp: an ultra-fast all-in-one FASTQ preprocessor. Bioinformatics. 2018;34(17):i884-i90.
26. Love MI, Huber W, Anders S. Moderated estimation of fold change and dispersion for RNA-seq data with DESeq2. Genome Biology. 2014;15(12):550.
27. Verheijen MCT, Meier MJ, Asensio JO, Gant TW, Tong W, Yauk CL, et al. R-ODAF: Omics data analysis framework for regulatory application. Regulatory Toxicology and Pharmacology. 2022;131:105143.
28. Yu G. Thirteen years of clusterProfiler. The Innovation. 2024;5(6):100722.
29. Doncheva NT, Morris JH, Gorodkin J, Jensen LJ. Cytoscape StringApp: Network Analysis and Visualization of Proteomics Data. J Proteome Res. 2019;18(2):623-32.
30. Shannon P, Markiel A, Ozier O, Baliga NS, Wang JT, Ramage D, et al. Cytoscape: a software environment for integrated models of biomolecular interaction networks. Genome Res. 2003;13(11):2498-504.
31. Gustavsen JA, Pai S, Isserlin R, Demchak B, Pico AR. RCy3: Network biology using Cytoscape from within R. F1000Res. 2019;8:1774.
32. Rezende LMTd, Soares LL, Drummond FR, Suarez PZ, Leite L, Rodrigues JA, et al. Is the Wistar Rat a more Suitable Normotensive Control for SHR to Test Blood Pressure and Cardiac Structure and Function? International Journal of Cardiovascular Sciences. 2021;35(2):161-71.
33. Sierksma AS, Prickaerts J, Chouliaras L, Rostamian S, Delbroek L, Rutten BP, et al. Behavioral and neurobiological effects of prenatal stress exposure in male and female APPswe/PS1dE9 mice. Neurobiol Aging. 2013;34(1):319-37.
34. Yang S, Webb AJS. Associations between neurovascular coupling and cerebral small vessel disease: A systematic review and meta-analysis. Eur Stroke J. 2023;8(4):895-903.
35. Zehendner CM, Tsohataridis S, Luhmann HJ, Yang JW. Developmental switch in neurovascular coupling in the immature rodent barrel cortex. PLoS One. 2013;8(11):e80749.
36. Mengler L, Khmelinskii A, Diedenhofen M, Po C, Staring M, Lelieveldt BPF, et al. Brain maturation of the adolescent rat cortex and striatum: Changes in volume and myelination. NeuroImage. 2014;84:35-44.
37. Branson HM. Normal myelination: a practical pictorial review. Neuroimaging Clin N Am. 2013;23(2):183-95.
38. Downes N, Mullins P. The development of myelin in the brain of the juvenile rat. Toxicol Pathol. 2014;42(5):913-22.
39. Suzuki K, Masawa N, Sakata N, Takatama M. Pathologic evidence of microvascular rarefaction in the brain of renal hypertensive rats. Journal of Stroke and Cerebrovascular Diseases. 2003;12(1):8-16.
40. Liu Y, Chen D, Smith A, Ye Q, Gao Y, Zhang W. Three-dimensional remodeling of functional cerebrovascular architecture and gliovascular unit in leptin receptor-deficient mice. J Cereb Blood Flow Metab. 2021;41(7):1547-62.
41. Cao R, Li J, Zhang C, Zuo Z, Hu S. Photoacoustic microscopy of obesity-induced cerebrovascular alterations. Neuroimage. 2019;188:369-79.

42. Filosa JA, Yao X, Rath G. TRPV4 and the regulation of vascular tone. J Cardiovasc Pharmacol. 2013;61(2):113-9.
43. Kondapalli NB, Katari V, Dalal K, Paruchuri S, Thodeti CK. Angiotensin II induces endothelial dysfunction and vascular remodeling by downregulating TRPV4 channels. J Mol Cell Cardiol Plus. 2023;6.
44. Luo H, Declèves X, Cisternino S. TRPV in the Brain Gliovascular Unit: Prospective Targets in Therapy. Pharmaceutics. 2021;13(3).
45. Matin N, Fisher C, Jackson WF, Dorrance AM. Bilateral common carotid artery stenosis in normotensive rats impairs endothelium-dependent dilation of parenchymal arterioles. Am J Physiol Heart Circ Physiol. 2016;310(10):H1321-9.
46. Diaz-Otero JM, Yen TC, Ahmad A, Laimon-Thomson E, Abolibdeh B, Kelly K, et al. TRPV4 channels are important regulators of parenchymal arteriole dilation and cognitive function. Microcirculation. 2019;26(6):e12535.
47. Dabravolski SA, Sukhorukov VN, Kalmykov VA, Grechko AV, Shakhpazyan NK, Orekhov AN. The Role of KLF2 in the Regulation of Atherosclerosis Development and Potential Use of KLF2-Targeted Therapy. Biomedicines. 2022;10(2).
48. Fang X, Zhong X, Yu G, Shao S, Yang Q. Vascular protective effects of KLF2 on Aβ-induced toxicity: Implications for Alzheimer's disease. Brain Res. 2017;1663:174-83.
49. Zhang X, Zhang J, Tang X, Zhou C, Yin K-J. Krüppel-like transcription factors in vascular biology and cerebrovascular diseases. 2019;2.
50. Liu L, Guo M, Lv X, Wang Z, Yang J, Li Y, et al. Role of TRPV4 in Vascular Function. Front Mol Biosci. 2021;8:677661.
51. Goyal N, Skrdla P, Schroyer R, Kumar S, Fernando D, Oughton A, et al. Clinical Pharmacokinetics, Safety, and Tolerability of a Novel, First-in-Class TRPV4 Ion Channel Inhibitor, GSK2798745, in Healthy and Heart Failure Subjects. Am J Cardiovasc Drugs. 2019;19(3):335-42.
52. Stewart GM, Johnson BD, Sprecher DL, Reddy YNV, Obokata M, Goldsmith S, et al. Targeting pulmonary capillary permeability to reduce lung congestion in heart failure: a randomized, controlled pilot trial. Eur J Heart Fail. 2020;22(9):1641-5.

808 ***Figure 1: Progression of systolic blood pressure, blood glucose and triglyceride levels in ZSF1 Obese vs Lean***
809 ***rats.*** *(A) Systolic blood pressure of Lean (open circles) and Obese (filled circles) ZSF1 rats (normotensive value*
810 *t=120 mmHg, dashed line (32)): 2-way ANOVA (p_{age}<0.0001, p_{group}=0.01, $p_{age\ x\ group}$=0.03). (B) Fasted blood glucose*
811 *(FBG) levels (t=100 mg/dl; dashed line): mixed effects (p_{age}=0.56, p_{group}<0.0001, $p_{age\ x\ group}$=0.0006). (C) Non-fasted*
812 *blood triglycerides levels: 2-way ANOVA (p_{age}<0.0001, p_{group}<0.0001, $p_{age\ x\ group}$<0.0001). Sidak's multiple*
813 *comparisons test: *p<0.05; **p<0.01; ***p<0.001 ****p<0.0001. n=14-15/group.*

814

815 ***Figure 2: In vivo assessment of cardiac function in ZSF1 rats at different time points using echocardiography.***
816 *(A) Ratio of early and late mitral inflow peak velocity (E/A ratio; mixed effects: p_{age}=0.66, p_{group}<0.0001, $p_{age\ x}$*
817 *$_{group}$=0.0008), (B) isovolumetric relaxation time (IVRT mixed effects: p_{age}=0.13, p_{group}=0.013, $p_{age\ x\ group}$=0.27),*
818 *(C) deceleration time (mixed effects: p_{age}=0.06, p_{group}=0.0079, $p_{age\ x\ group}$=0.0173), (D) pulmonary peak velocities*
819 *(mixed effects: p_{age}<0.0001, p_{group}<0.0001, $p_{age\ x\ group}$<0.0001), (E) aortic peak velocities (mixed effects:*
820 *p_{age}<0.0001, p_{group}=0.0189, $p_{age\ x\ group}$<0.0001), and (F) anterior left ventricular (LV) wall thickness (mixed effects:*
821 *p_{age}=0.0013, p_{group}=0.0002, $p_{age\ x\ group}$=0.35) in Lean (open circles; white bars) and Obese (filled circles; grey bars)*
822 *ZSF1 rats. Sidak's multiple comparisons test: *p<0.05, **p<0.01, ***p<0.001, ****p<0.0001. n=5-14/group.*

823

824 ***Figure 3: Anxiety and cognitive function of ZSF1 rats at three time points.*** *Lean (open circles; white bars) and*
825 *Obese (filled circles; grey bars) ZSF1 rats underwent a series of behavioural tests, including (A) elevated zero maze*
826 *(EZM), (B) Y-maze alternation task (YM), (C) Barnes maze (BM) and (E) novel object recognition task (NORT) to*
827 *assess anxiety, working memory, long term spatial learning/memory, and short-term memory, respectively.*
828 *(E) EZM (2-way ANOVA: p_{age}=0.12, p_{group}=0.0006, $p_{age\ x\ group}$=0.0012); (F) YM, percentage of alternations (mixed*
829 *effects: p_{age}=0.0019, p_{group}=0.60, $p_{age\ x\ group}$=0.83, (33)), (G) YM, number of entries (mixed effects: p_{age}<0.0001,*
830 *p_{group}<0.0001, $p_{age\ x\ group}$=0.15); (H-J) BM, spatial learning at 14-16w (2-way ANOVA: p_{age}<0.0001, p_{group}=0.46, p_{age}*
831 *$_{x\ group}$=0.35), 20-22w (2-way ANOVA: p_{age}<0.0001, p_{group}=0.01, $p_{age\ x\ group}$<0.0001), and 30-32w (mixed effects:*
832 *p_{age}<0.0001, p_{group}=0.03, $p_{age\ x\ group}$<0.0001), (K) BM 30-second probe trial, long-term memory (mixed effects:*
833 *p_{age}=0.30, p_{group}=0.04, $p_{age\ x\ group}$=0.84), (L) BM, reversal learning (mixed effects: p_{age}<0.0001, p_{group}=0.84, $p_{age\ x}$*
834 *$_{group}$=0.01); (M) NORT (mixed effects: p_{age}=0.43, p_{group}=0.0019, $p_{age\ x\ group}$=0.29); Sidak's multiple comparisons test:*

835 **p<0.05, **p<0.01, ***p<0.001, ****p<0.0001. Single t-test: #p<0.05 vs (F) alternation rate of 50% (dotted line,)*
836 *and (M) d2=0 (33). EZM: n=14-15/group, YM: 13-15/group; NORT: n=4-10/group; BM: 13-15/group. Illustrations*
837 *in panels A-D were created using BioRender.com.*

838 ***Figure 4: Brain atrophy, white matter content and integrity in ZSF1 and Wistar rats**. (A) Representative image*
839 *of a brain section stained with Luxol fast blue (left image) with delineation of the pericallosal area (red dotted*
840 *line) and whole brain area (green dotted line); representative image depicting retardance (middle image) and*
841 *dispersion (right image). Scale bar = 1 mm. (B) Brain weight to tibia length from Lean (open circles; white bars)*
842 *and Obese (filled circles; grey bars) ZSF1 rats (2-way ANOVA: p_{age}<0.0001, p_{group}<0.0001, $p_{age\ x\ group}$=0.13). (C)*
843 *Relative proportion of the pericallosal area over whole brain tissue (2-way ANOVA: p_{age}<0.0001, p_{group}=0.03, p_{age}*
844 *$_{x\ group}$=0.13). Relative Luxol Fast Blue intensity of the (D) pericallosal area (2-way ANOVA: p_{age}=0,69, p_{group}=0,04,*
845 *$p_{age\ x\ group}$=0.98) and (E) striatum area (2-way ANOVA: p_{age}=0,09, p_{group}=0,02, $p_{age\ x\ group}$=0.79). Relative retardance*
846 *of the (F) pericallosal area (2-way ANOVA: p_{age}<0.0001, p_{group}=0,62, $p_{age\ x\ group}$=0.92) and (G) striatum area (2-way*
847 *ANOVA: p_{age}<0.001, p_{group}=0,80, $p_{age\ x\ group}$=0.95). Relative dispersion of the (H) pericallosal area (2-way ANOVA:*
848 *p_{age}=0,49, p_{group}=0,17, $p_{age\ x\ group}$=0.93) and (I) striatum area (2-way ANOVA: p_{age}<0.0001, p_{group}=0,051, $p_{age\ x}$*
849 *$_{group}$=0.49). Sidak's multiple comparisons test: *p<0.05, **p<0.01, ***p<0.001, ****p<0.0001. Single t-test:*
850 *#p<0.05 vs (B) Wistar (black dotted line) = 0.04 ± 0.0008 g/mm, vs (C) Wistar = 8.19 ± 0.41 %. vs (D) Wistar = 45.8*
851 *± 1.4 %. %. vs (E) Wistar = 27.6 ± 1.5 %. %. vs (F) Wistar = 7.5 ± 0.3 %. %. vs (G) Wistar = 2.1 ± 0.1 %. %. vs (H)*
852 *Wistar = 88.2 ± 0.9 %. %. vs (I) Wistar = 51.9 ± 3.0 %. n=8-10/group.*

853 ***Figure 5: Cerebral blood flow and neurovascular coupling in ZSF1 and Wistar rats.** (A) Schematic overview of*
854 *thinned skull window surgeries and laser speckle contrast imaging over the barrel cortex area. (B-C)*
855 *Representative images of cerebral blood flow (CBF) before and during whisker stimulation. (D) Baseline CBF (2-*
856 *way ANOVA: p_{age}=0.02, p_{group}=0.20, $p_{age\ x\ group}$=0.55) and (E) Neurovascular coupling (2-way ANOVA: p_{age}<0.0001,*
857 *p_{group}=0.002, $p_{age\ x\ group}$=0.04) of ZSF1 rats were assessed at three different time points and compared to*
858 *normotensive Wistars rats (20-21w, dotted line). Sidak's multiple comparisons test: *P<0.05, **p<0.01,*
859 ****P<0.001, ****P<0.0001. Single t-test: #p<0.05 vs (D) Wistar (20-21w) = 206 ± 10 PU and (E) Wistar = 23.42 ±*
860 *0.81 %. n=10-14/group. PU = perfusion units. Scale bar = 100 µm. Illustration in panel A was created using*
861 *BioRender.com.*

862 ***Figure 6: Cerebral microvasculature and BBB permeability in ZSF1 and Wistar rats.*** *(A-B) Representative images*
863 *(maximal projection) of lectin-stained brain sections in the deep cortical area prior to analysis, and (C-D) after*
864 *analysis in Angiotool (Vessel width = yellow line; Vessel skeleton = red line; Branching points = blue dots).*
865 *(E) Cortical vascular density (mixed effects: p_{age}=0.12, p_{group}=0.02, $p_{age\ x\ group}$=0.03), and (F) Branching points (mixed*
866 *effects: p_{age}=0.10, p_{group}=0.55, $p_{age\ x\ group}$=0.61) in Lean (open circles; white bars) and Obese (filled circles; grey*
867 *bars) ZSF1 rats. (G-J) Representative images of IgG leakages in brain sections from ZSF1 rats. (K) Number of IgG*
868 *leakages (2-way ANOVA: p_{age}=0.31, p_{group}=0.06, $p_{age\ x\ group}$=0.42), and (L) IgG leakage size (2-way ANOVA:*
869 *p_{age}=0.0026, p_{group}=0.02, $p_{age\ x\ group}$=0.09). Sidak's multiple comparisons test: **p<0.01, ***p<0.001. Single t-test:*
870 *#p<0.05 vs (E) Wistar (22-23w, dotted line) = 9.32 ± 0.63 %, (F) Wistar (22-23w, dotted line) = 349 ± 63*
871 *junctions/mm^2, (K) Wistar (22-23w, dotted line) = 6.46 ± 1.44, and (F) Wistar (22-23w, dotted line) = 2057 ± 392.8*
872 *µm^2. n=4-10/group.*

873

874 ***Figure 7: Transcriptomic regulation within brain microvessels of ZSF1 rats****. (A-C) Volcano plots of all genes in the*
875 *dataset, p-value<0.05 and fold change>1.5 (|log2FC|>0,58). The total number of differentially expressed genes*
876 *(DEGs, Obese vs Lean) is 98 at 8-9w, 254 at 22-23w, and 487 at 34-35w.(D) Biological processes enriched within*
877 *the dataset of 22-23w clustered into functional categories. (E) Protein-protein interaction network within the GO*
878 *term GO:0003018 'vascular process in circulatory system': DEGs (yellow circles) are represented with their direct*
879 *connections. (F) Heatmap showing the expression profiles of DEGs within the GO term GO:0003018 at 22-23w*
880 *and 34-35w: High-Temperature Requirement A Serine Peptidase 1 (Htra1), Kruppel-Like Factor 2 (Klf2), Transient*
881 *Receptor Potential Vanilloid 4 (Trpv4), Angiotensin-Converting Enzym (Ace), Matrix Metallopeptidase 2 (Mmp2,)*
882 *5-Hydroxytryptamine (Serotonin) Receptor 2C (Htr2c), Superoxide Dismutase 3 (Sod3), and Plasmalemma Vesicle*
883 *Associated Protein (Pvlap). n=4/group. Colour legend: red = upregulated, blue = downregulated.*

884 ***Figure 8: Multiplex detection of target probes Klf2 and Trpv4 in paraffin-embedded ZSF1 rat brains.***
885 *(A-D) Representative images (maximal projection) of KLF2 (green) and TRPV4 (red) RNA transcripts inside lectin-*
886 *stained vessels (grey) in the deep cortical area of Lean and Obese ZSF1 rat brains at 22-23 and 34-35 weeks of*
887 *age. (E) The number of Klf2 transcripts per 100µm vessels (2-way ANOVA: p_{age}=0.87, p_{group}=0.01, $p_{age\ x}$*
888 *$_{group}$=0.0009) and (F) total Klf2 signal intensity per µm^3 vessels (2-way ANOVA: p_{age}=0.99, p_{group}0.01, $p_{age\ x}$*
889 *$_{group}$=0.0005) in Lean (open circles; white bars) and Obese (filled circles; grey bars) ZSF1 rats; (I) Number of Trpv4*

890 *transcripts per 100µm vessels (2-way ANOVA: p_{age}=0.67, p_{group}=0.27, $p_{age\ x\ group}$=0.02), (J) Total intensity of Trpv4*

891 *signal per µm^3 vessels (2-way ANOVA: p_{group}=0.27, p_{age}=0.46, $p_{group\ x\ age}$=0.04). Sidak's multiple comparisons test:*

892 **p<0.05, ***p<0.001. n=10-13 FOVs/group.*

893

894 Figure 1

895

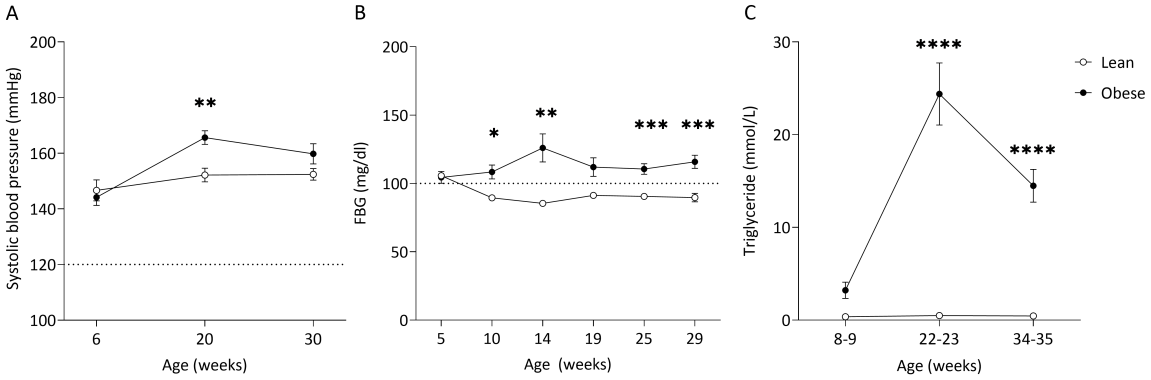

896

Figure 2

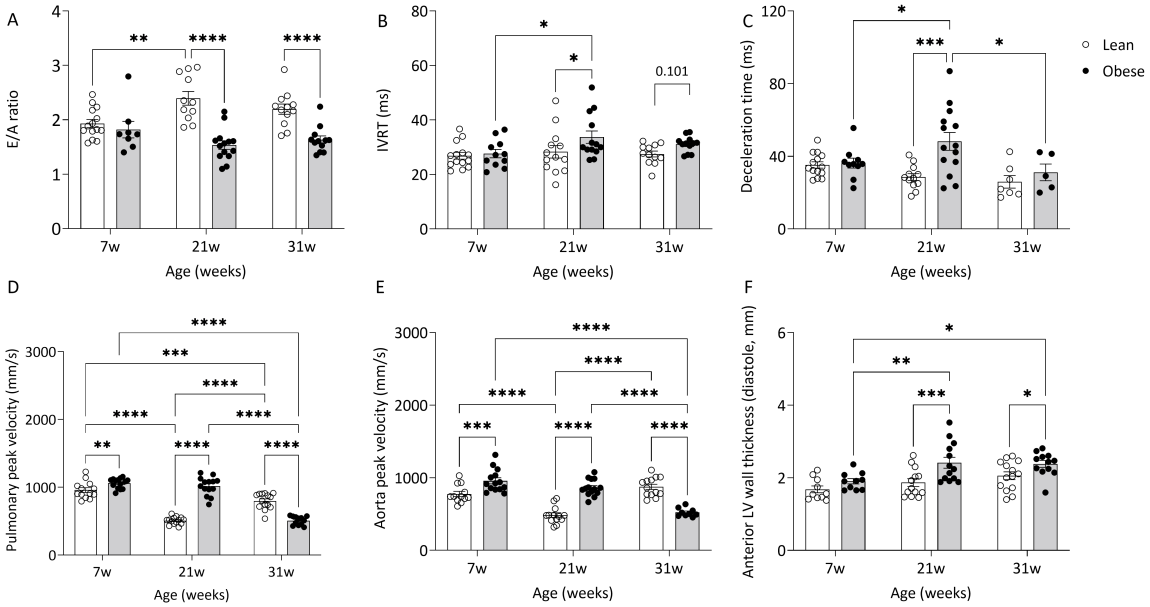
A
E/A ratio
Age (weeks)
7w
21w
31w
B
IVRT (ms)
0.101
C
Deceleration time (ms)
Lean
Obese
D
Pulmonary peak velocity (mm/s)
E
Aorta peak velocity (mm/s)
F
Anterior LV wall thickness (diastole, mm)

Figure 3

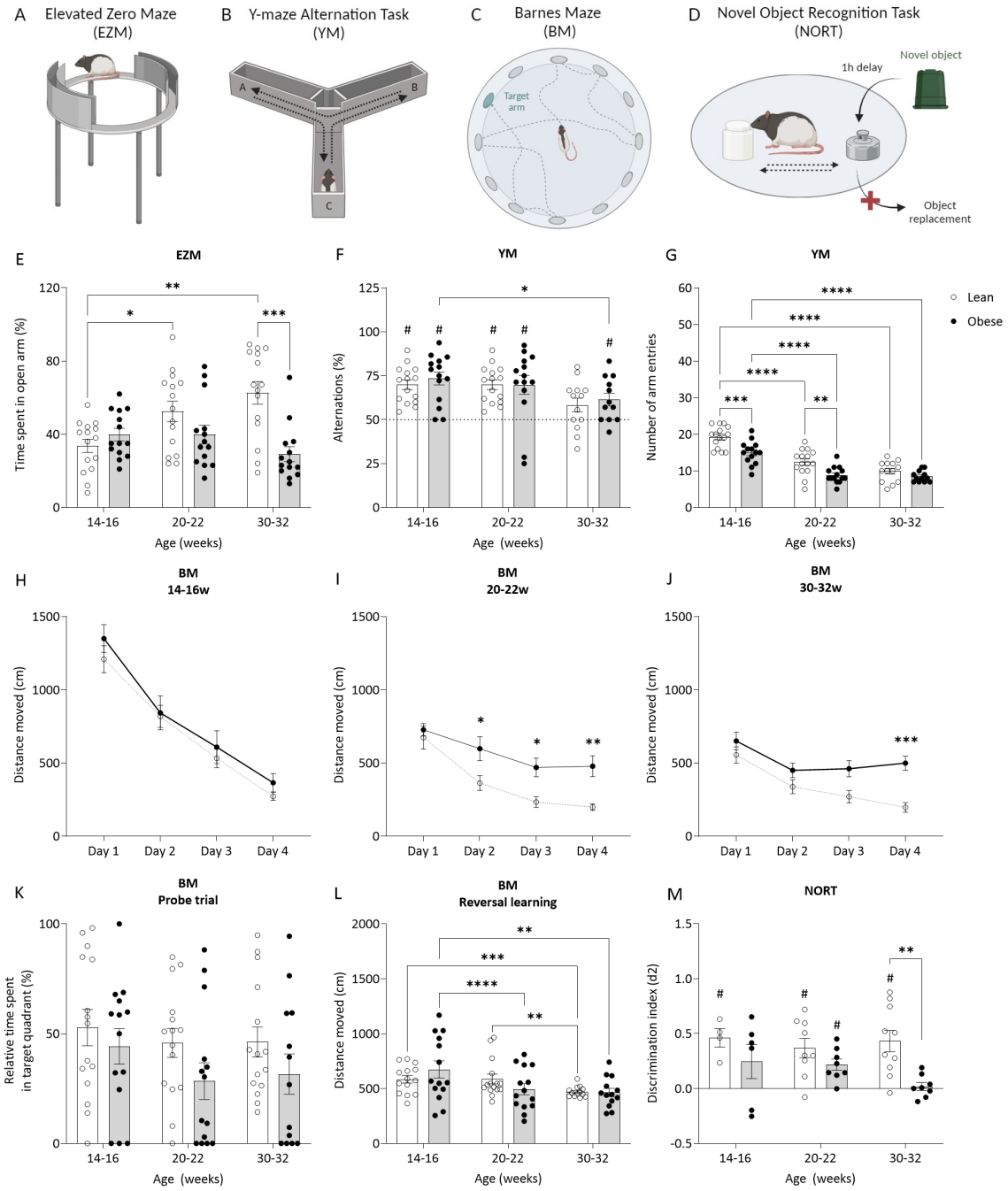
A Elevated Zero Maze (EZM)
B Y-maze Alternation Task (YM)
C Barnes Maze (BM)
D Novel Object Recognition Task (NORT)
Target arm
1h delay
Novel object
Object replacement
E EZM
Time spent in open arm (%)
F YM
Alternations (%)
G YM
Number of arm entries
Lean
Obese
Age (weeks)
14-16
20-22
30-32
H BM 14-16w
I BM 20-22w
J BM 30-32w
Distance moved (cm)
Day 1
Day 2
Day 3
Day 4
K BM Probe trial
Relative time spent in target quadrant (%)
L BM Reversal learning
M NORT
Discrimination index (d2)

Figure 4

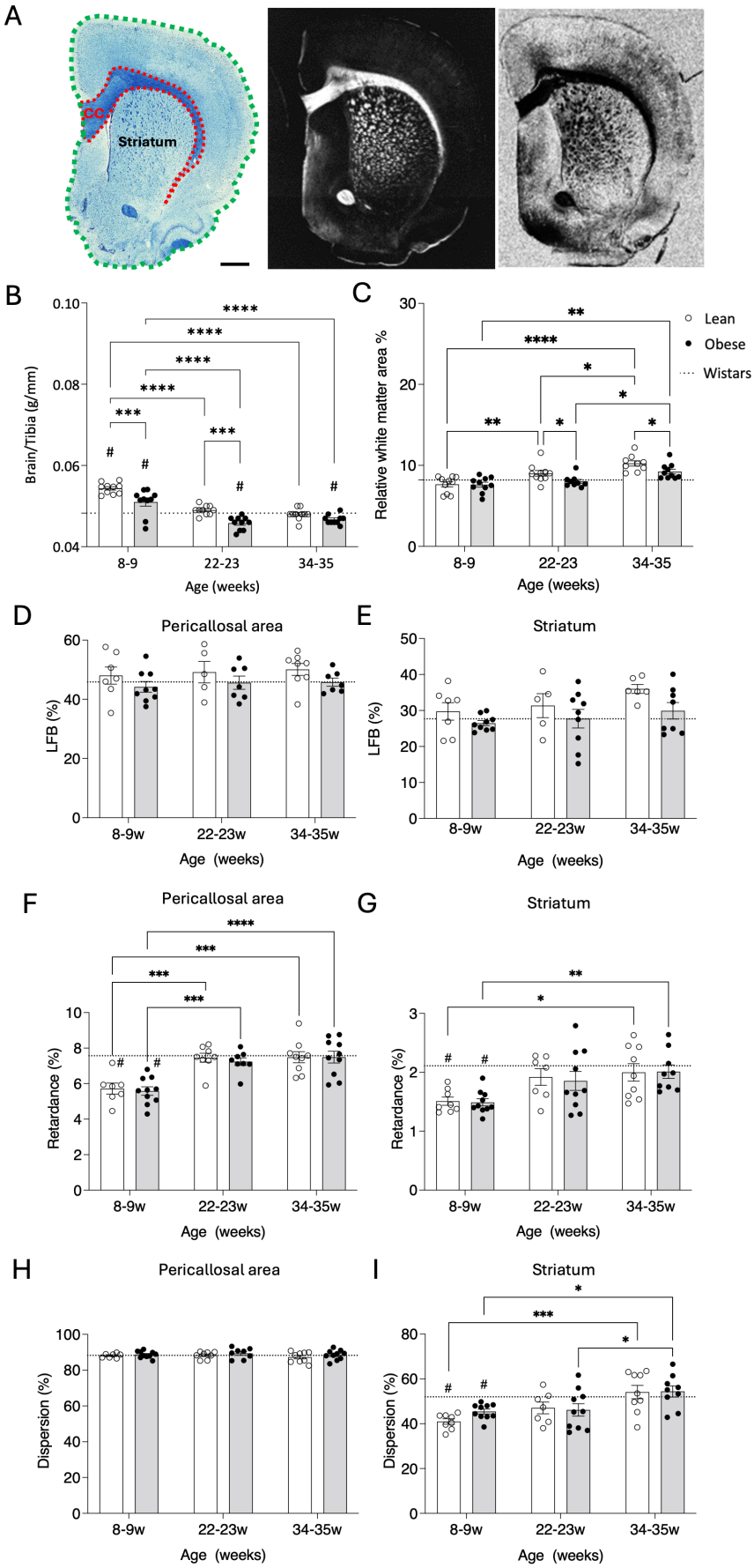
A
CC
Striatum
B
Brain/Tibia (g/mm)
Age (weeks)
8-9
22-23
34-35
C
Relative white matter area %
Lean
Obese
Wistars
D
Pericallosal area
LFB (%)
8-9w
22-23w
34-35w
E
Striatum
F
Retardance (%)
G
H
Dispersion (%)
I

Figure 5

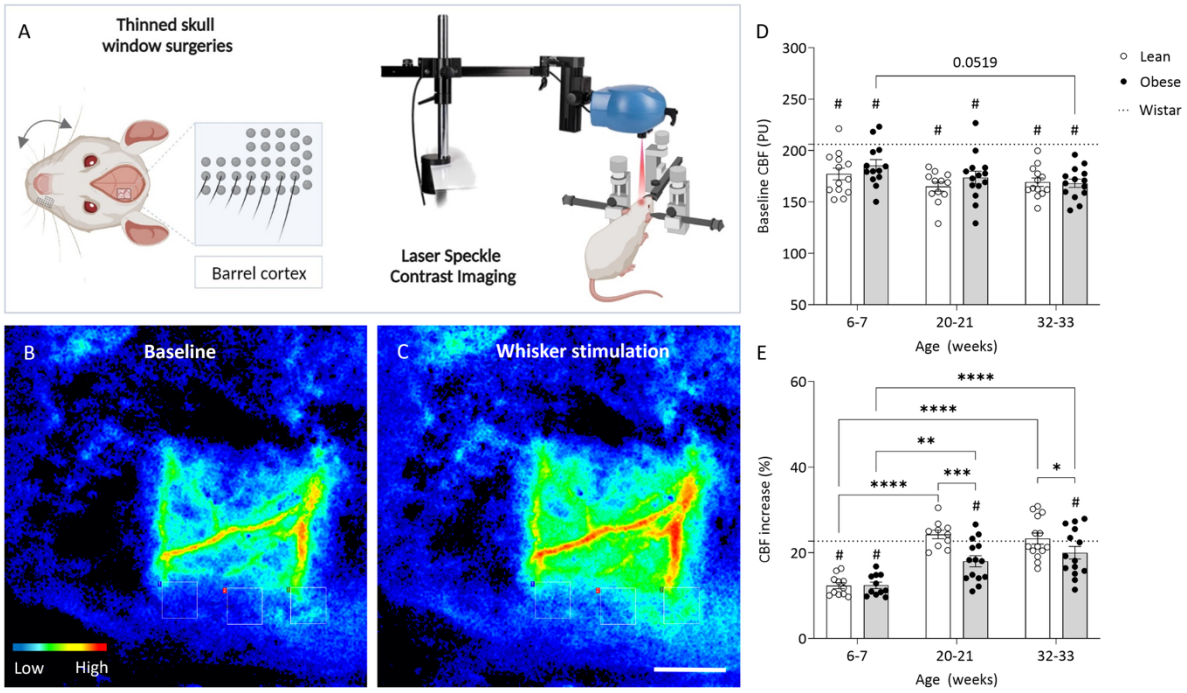
A
Thinned skull window surgeries
Barrel cortex
Laser Speckle Contrast Imaging
B
Baseline
Low
High
C
Whisker stimulation
D
Baseline CBF (PU)
0.0519
Lean
Obese
Wistar
6-7
20-21
32-33
Age (weeks)
E
CBF increase (%)
****
**
***
*
#

Figure 6

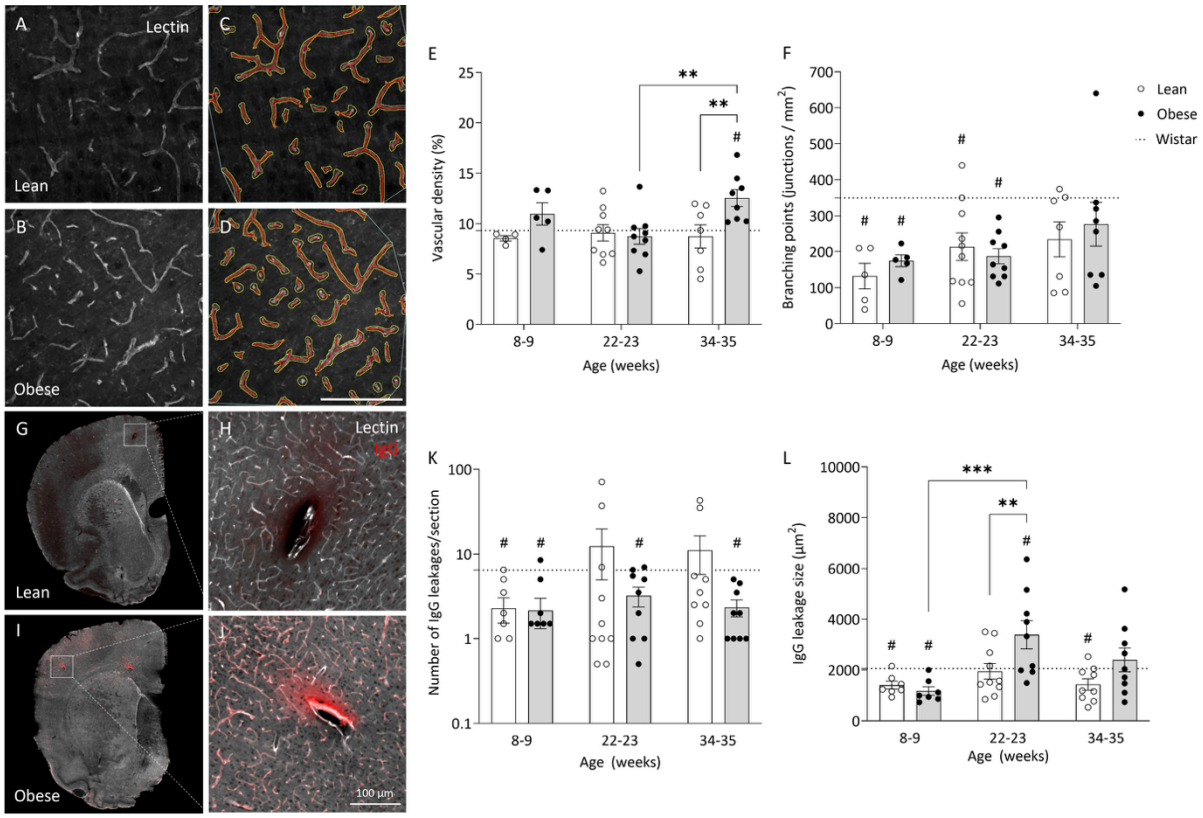
A
Lectin
Lean
C
B
Obese
D
E
Vascular density (%)
Age (weeks)
8-9
22-23
34-35
F
Branching points (junctions / mm²)
Lean
Obese
Wistar
G
Lean
H
Lectin
IgG
I
Obese
J
100 µm
K
Number of IgG leakages/section
L
IgG leakage size (µm²)

Figure 7

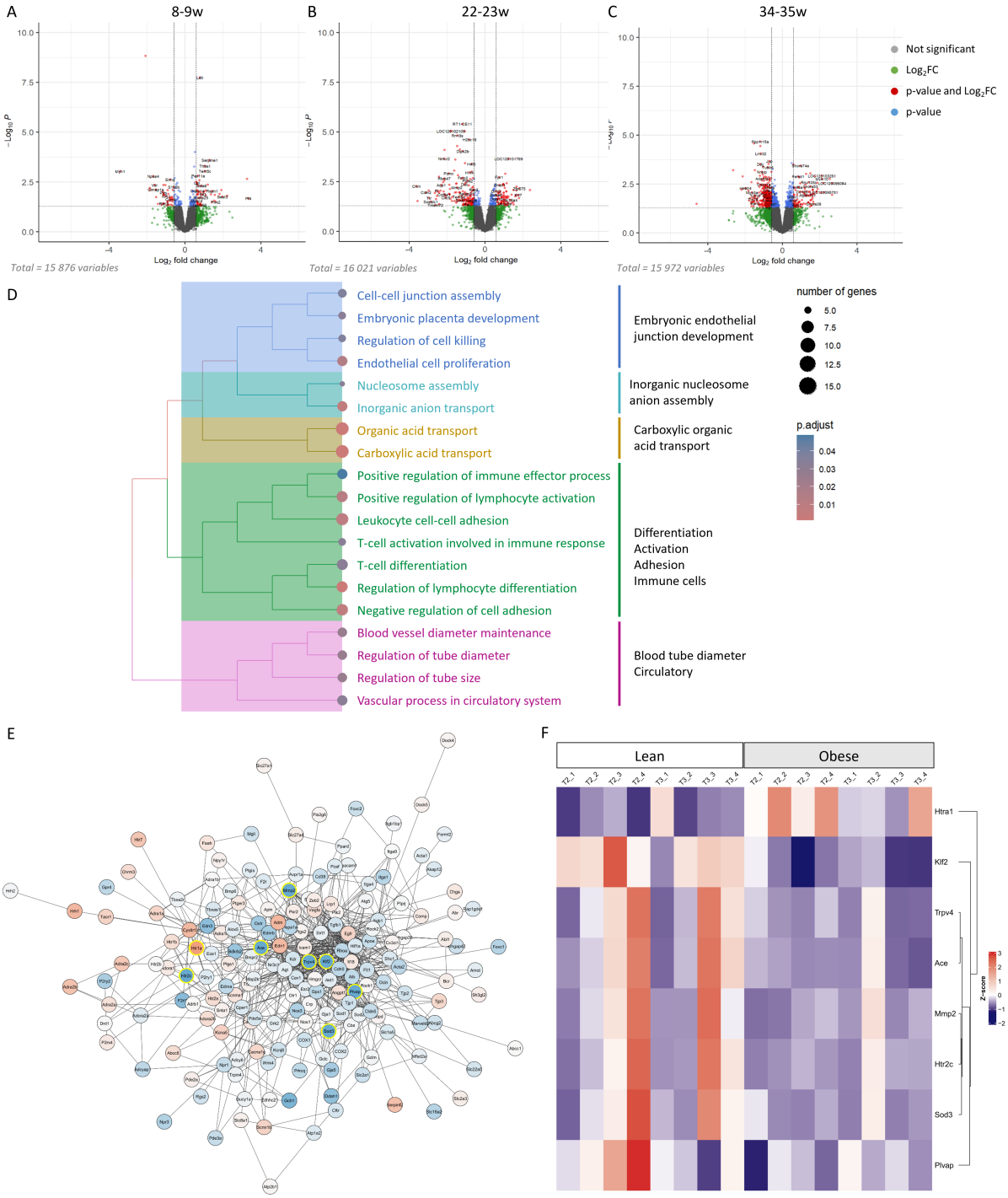
A
8-9w
B
22-23w
C
34-35w
Not significant
Log2FC
p-value and Log2FC
p-value
Log2 fold change
Total = 15 876 variables
Total = 16 021 variables
Total = 15 972 variables
D
Cell-cell junction assembly
Embryonic placenta development
Regulation of cell killing
Endothelial cell proliferation
Nucleosome assembly
Inorganic anion transport
Organic acid transport
Carboxylic acid transport
Positive regulation of immune effector process
Positive regulation of lymphocyte activation
Leukocyte cell-cell adhesion
T-cell activation involved in immune response
T-cell differentiation
Regulation of lymphocyte differentiation
Negative regulation of cell adhesion
Blood vessel diameter maintenance
Regulation of tube diameter
Regulation of tube size
Vascular process in circulatory system
Embryonic endothelial junction development
Inorganic nucleosome anion assembly
Carboxylic organic acid transport
Differentiation
Activation
Adhesion
Immune cells
Blood tube diameter
Circulatory
number of genes
p.adjust
E
F
Lean
Obese
Htra1
Klf2
Trpv4
Ace
Mmp2
Htr2c
Sod3
Plvap
Z-score

Figure 8

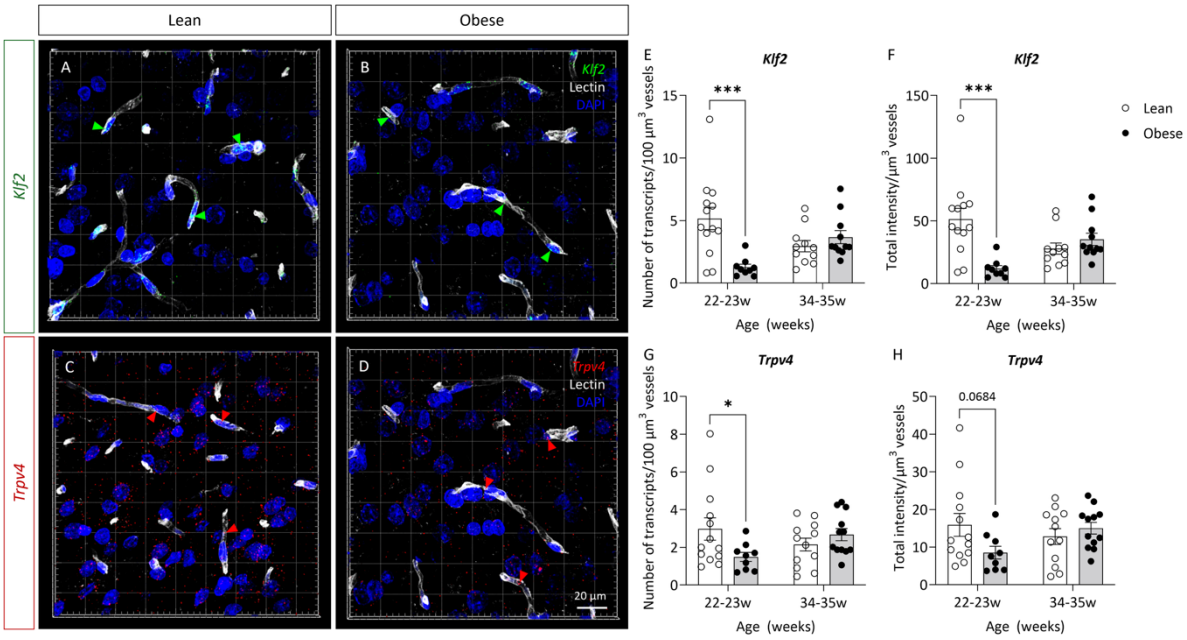
Lean
Obese
Klf2
Trpv4
A
B
C
D
Klf2
Lectin
DAPI
Trpv4
Lectin
DAPI
20 µm
E
Klf2
Number of transcripts/100 µm³ vessels
***
22-23w
34-35w
Age (weeks)
F
Klf2
Total intensity/µm³ vessels
***
Lean
Obese
G
Trpv4
Number of transcripts/100 µm³ vessels
*
H
Trpv4
Total intensity/µm³ vessels
0.0684

922 Figure S1

923

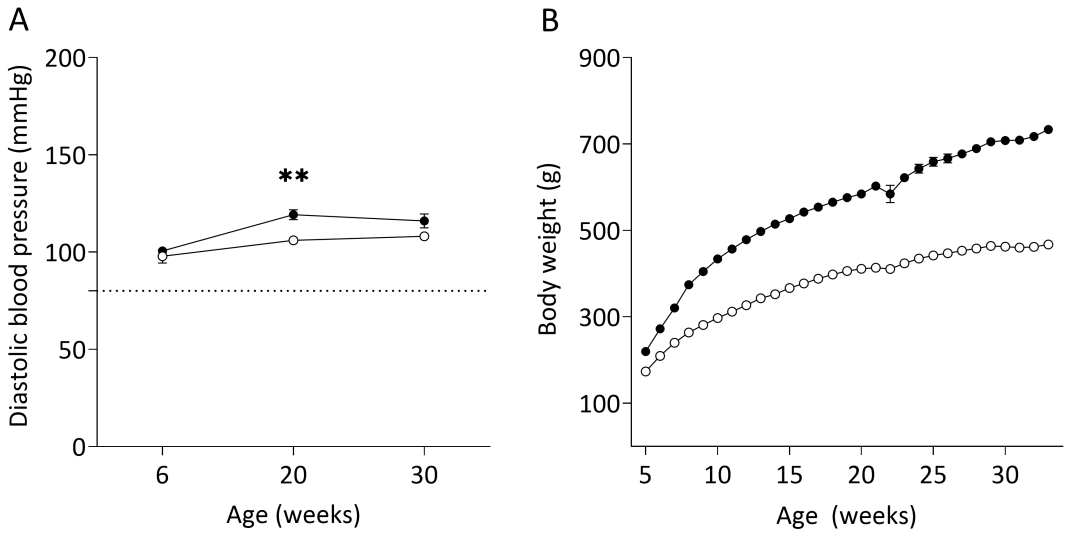

924

925

Figure S2

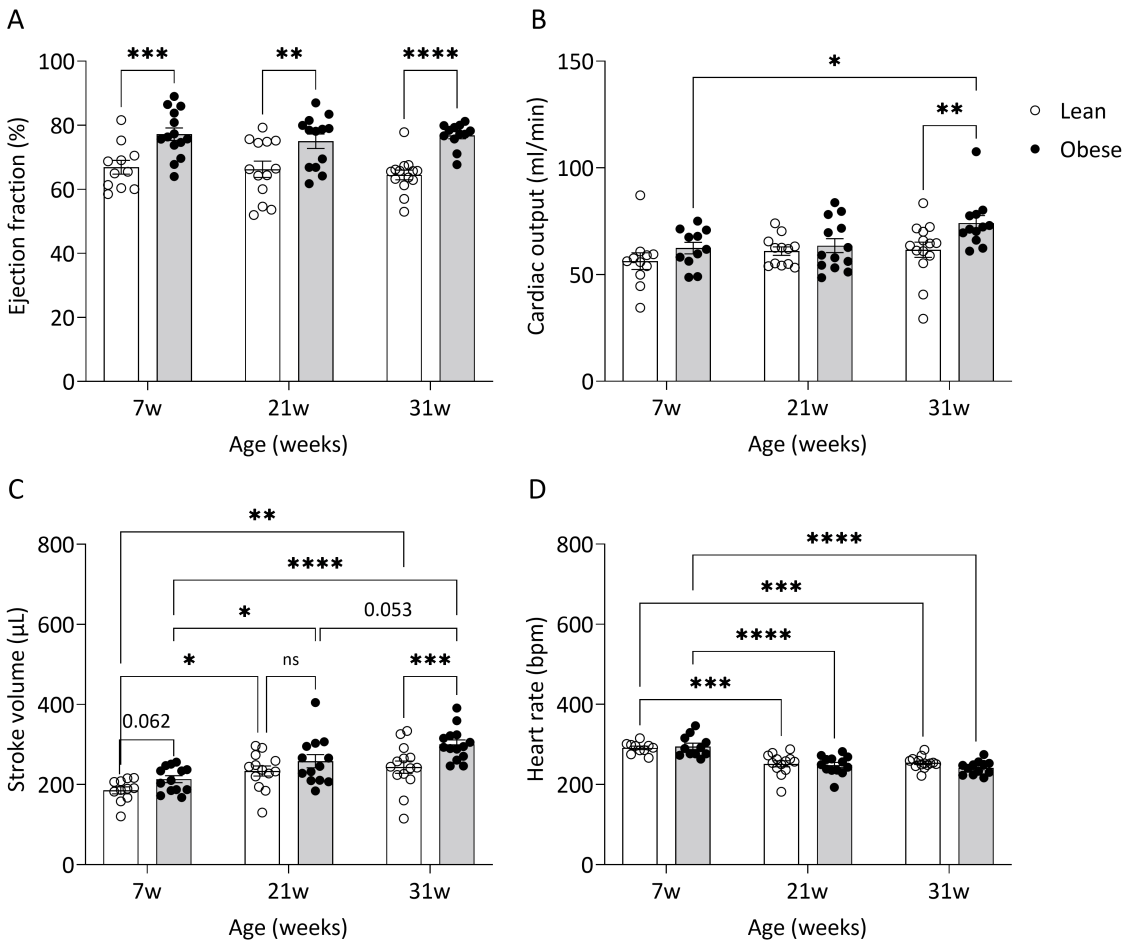
A
Ejection fraction (%)
100
80
60
40
20
0
***
**
****
7w
21w
31w
Age (weeks)
B
Cardiac output (ml/min)
150
100
50
0
*
**
7w
21w
31w
Age (weeks)
Lean
Obese
C
Stroke volume (µL)
800
600
400
200
0
**
****
*
0.053
*
ns
***
0.062
7w
21w
31w
Age (weeks)
D
Heart rate (bpm)
800
600
400
200
0
****
***
****
***
7w
21w
31w
Age (weeks)

Figure S3

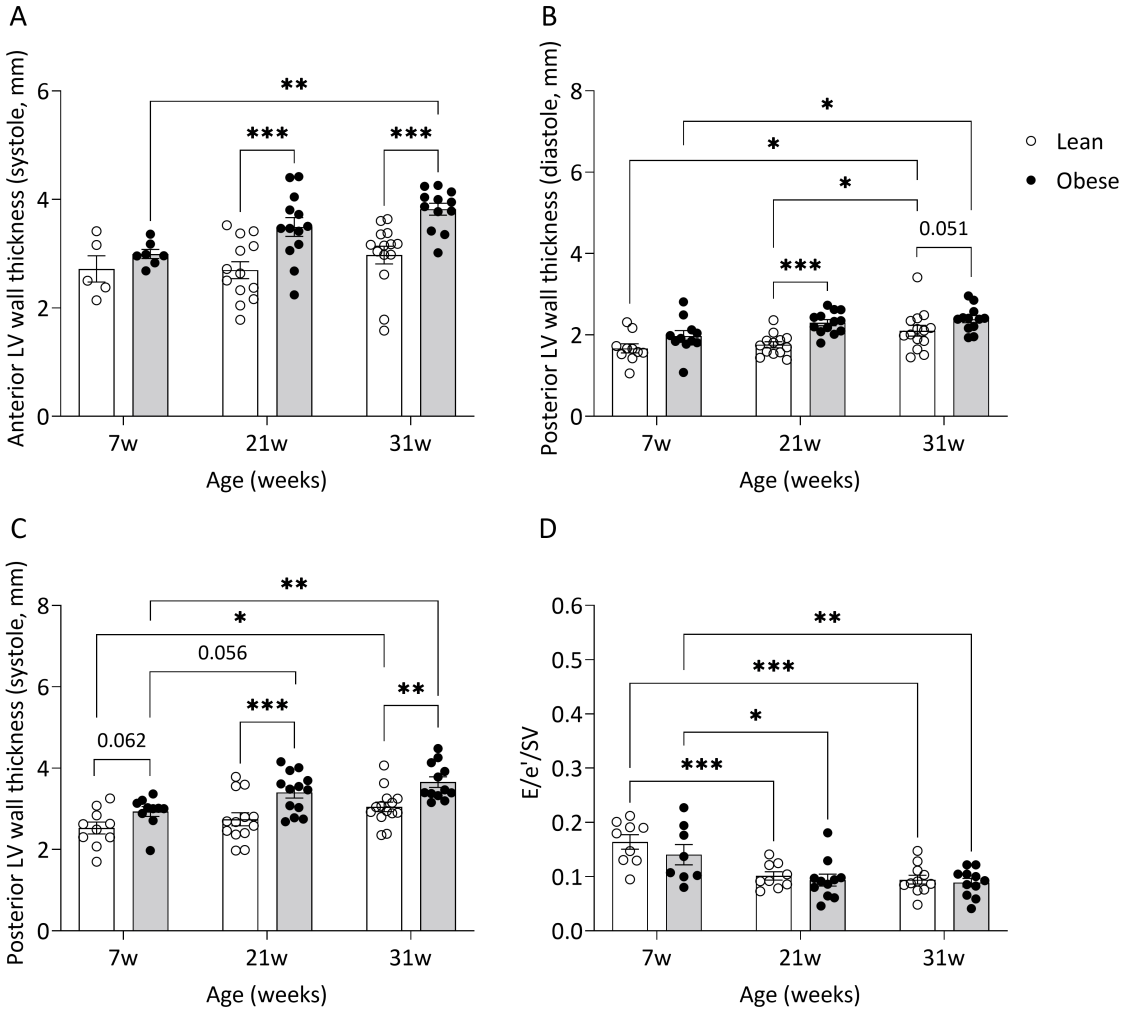
A
Anterior LV wall thickness (systole, mm)
Age (weeks)
7w
21w
31w
**
***
***
B
Posterior LV wall thickness (diastole, mm)
Age (weeks)
*
*
*
***
0.051
Lean
Obese
C
Posterior LV wall thickness (systole, mm)
Age (weeks)
**
*
0.056
***
**
0.062
D
E/e'/SV
Age (weeks)
**
***
*
***

934 Figure S4

935

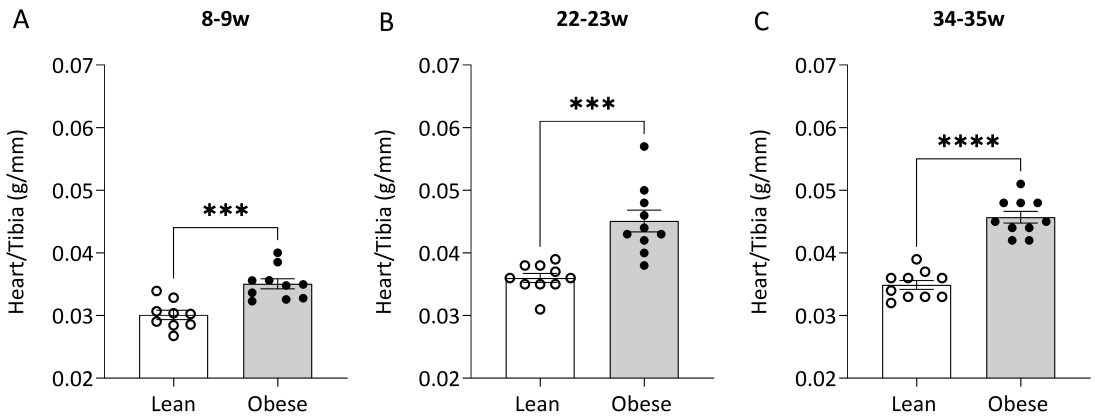

936

937

938 Figure S5

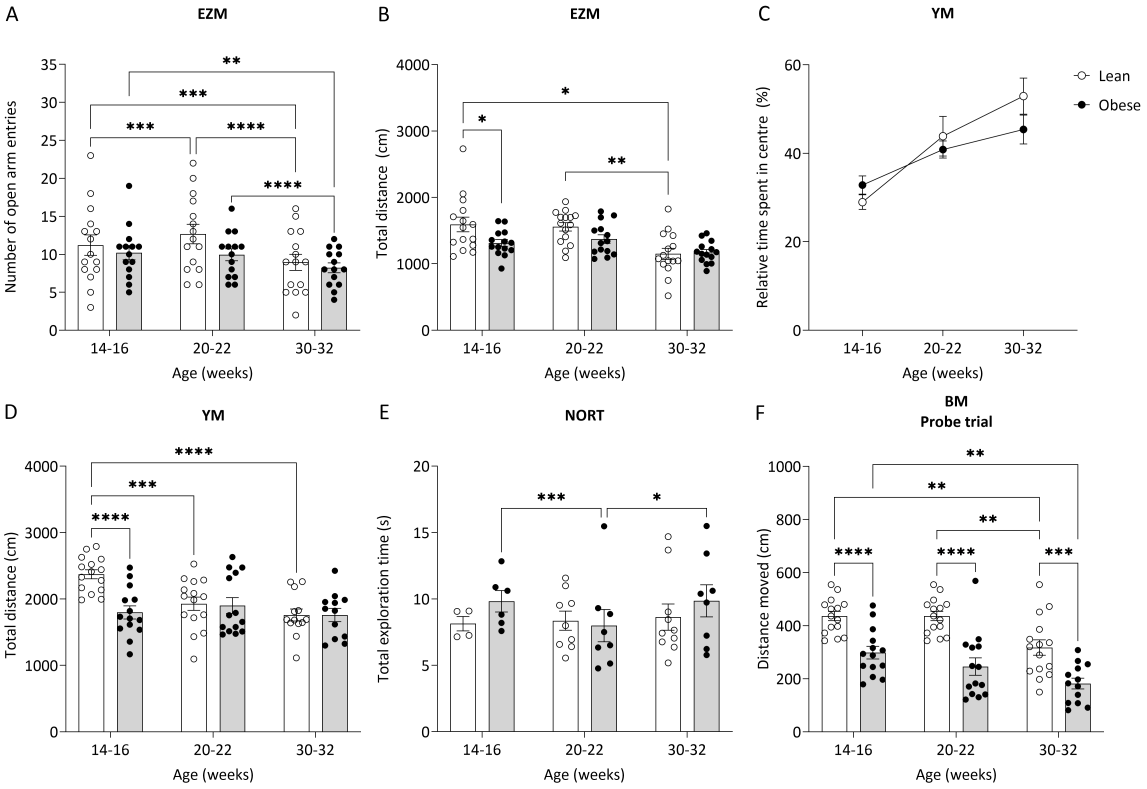

939

940

941

942

943 Figure S6

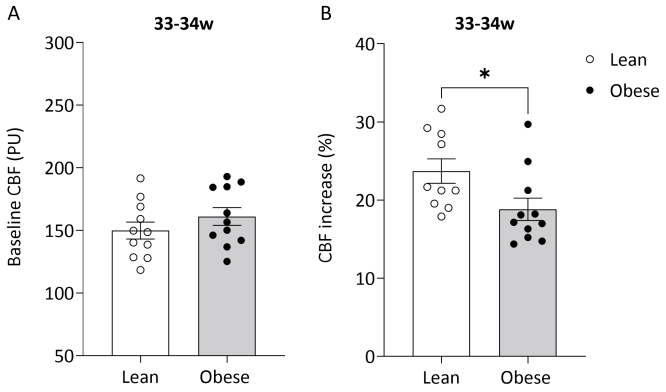

944

945

946

947 Figure S7

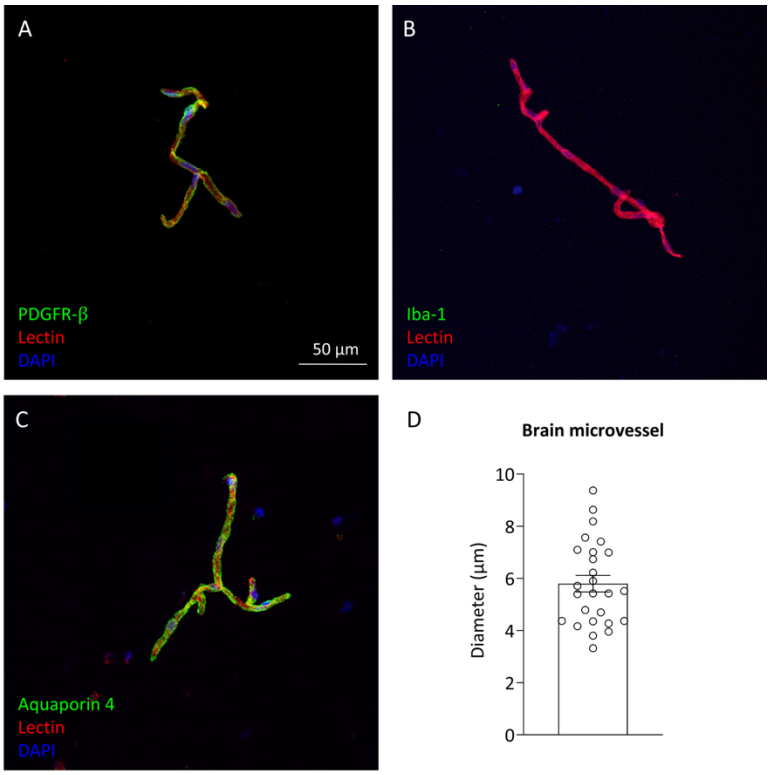

948

949

950

Figure S8

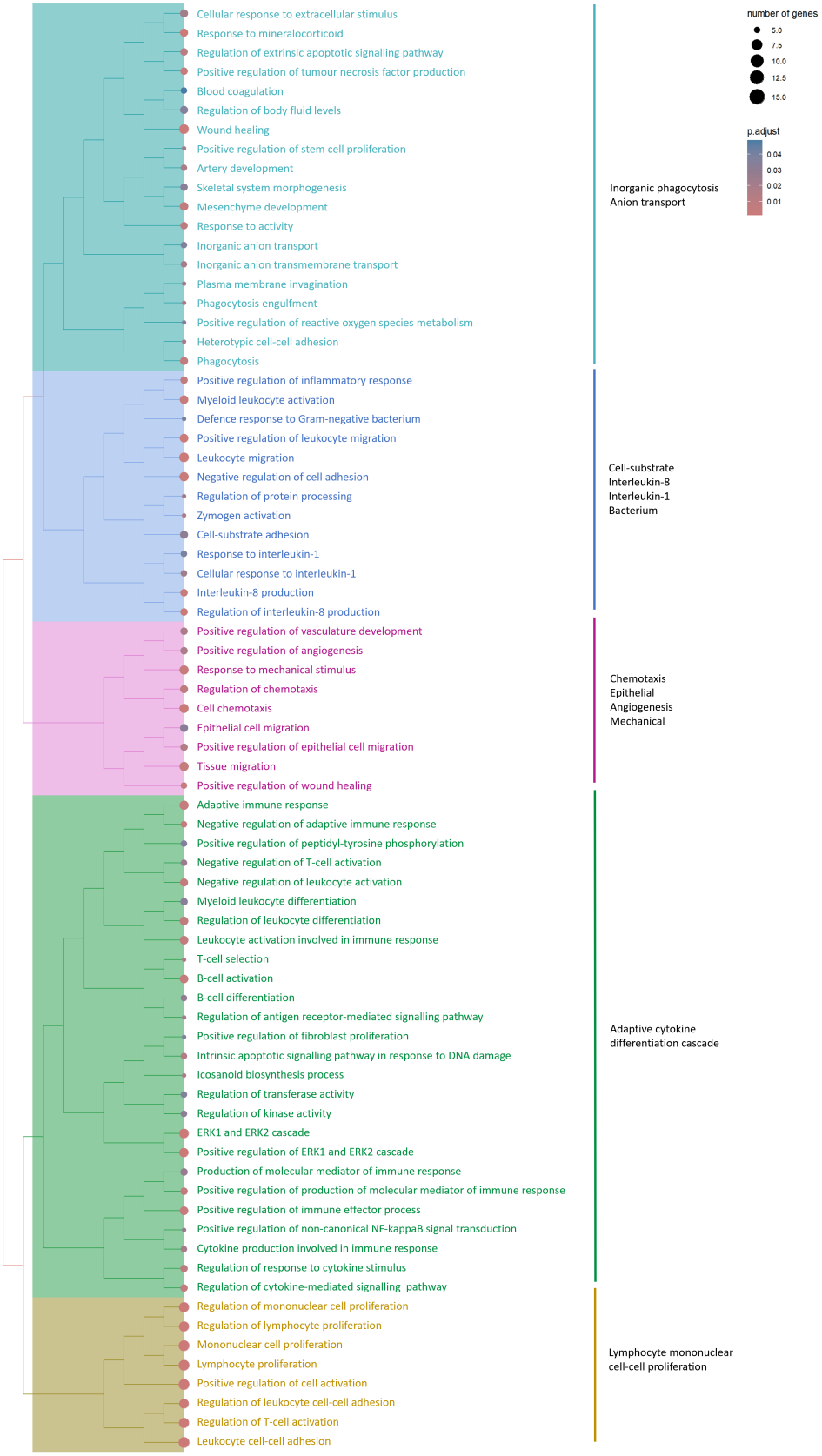
Cellular response to extracellular stimulus
Response to mineralocorticoid
Regulation of extrinsic apoptotic signalling pathway
Positive regulation of tumour necrosis factor production
Blood coagulation
Regulation of body fluid levels
Wound healing
Positive regulation of stem cell proliferation
Artery development
Skeletal system morphogenesis
Mesenchyme development
Response to activity
Inorganic anion transport
Inorganic anion transmembrane transport
Plasma membrane invagination
Phagocytosis engulfment
Positive regulation of reactive oxygen species metabolism
Heterotypic cell-cell adhesion
Phagocytosis
Positive regulation of inflammatory response
Myeloid leukocyte activation
Defence response to Gram-negative bacterium
Positive regulation of leukocyte migration
Leukocyte migration
Negative regulation of cell adhesion
Regulation of protein processing
Zymogen activation
Cell-substrate adhesion
Response to interleukin-1
Cellular response to interleukin-1
Interleukin-8 production
Regulation of interleukin-8 production
Positive regulation of vasculature development
Positive regulation of angiogenesis
Response to mechanical stimulus
Regulation of chemotaxis
Cell chemotaxis
Epithelial cell migration
Positive regulation of epithelial cell migration
Tissue migration
Positive regulation of wound healing
Adaptive immune response
Negative regulation of adaptive immune response
Positive regulation of peptidyl-tyrosine phosphorylation
Negative regulation of T-cell activation
Negative regulation of leukocyte activation
Myeloid leukocyte differentiation
Regulation of leukocyte differentiation
Leukocyte activation involved in immune response
T-cell selection
B-cell activation
B-cell differentiation
Regulation of antigen receptor-mediated signalling pathway
Positive regulation of fibroblast proliferation
Intrinsic apoptotic signalling pathway in response to DNA damage
Icosanoid biosynthesis process
Regulation of transferase activity
Regulation of kinase activity
ERK1 and ERK2 cascade
Positive regulation of ERK1 and ERK2 cascade
Production of molecular mediator of immune response
Positive regulation of production of molecular mediator of immune response
Positive regulation of immune effector process
Positive regulation of non-canonical NF-kappaB signal transduction
Cytokine production involved in immune response
Regulation of response to cytokine stimulus
Regulation of cytokine-mediated signalling pathway
Regulation of mononuclear cell proliferation
Regulation of lymphocyte proliferation
Mononuclear cell proliferation
Lymphocyte proliferation
Positive regulation of cell activation
Regulation of leukocyte cell-cell adhesion
Regulation of T-cell activation
Leukocyte cell-cell adhesion
number of genes
5.0
7.5
10.0
12.5
15.0
p.adjust
0.04
0.03
0.02
0.01
Inorganic phagocytosis
Anion transport
Cell-substrate
Interleukin-8
Interleukin-1
Bacterium
Chemotaxis
Epithelial
Angiogenesis
Mechanical
Adaptive cytokine
differentiation cascade
Lymphocyte mononuclear
cell-cell proliferation

Figure S9

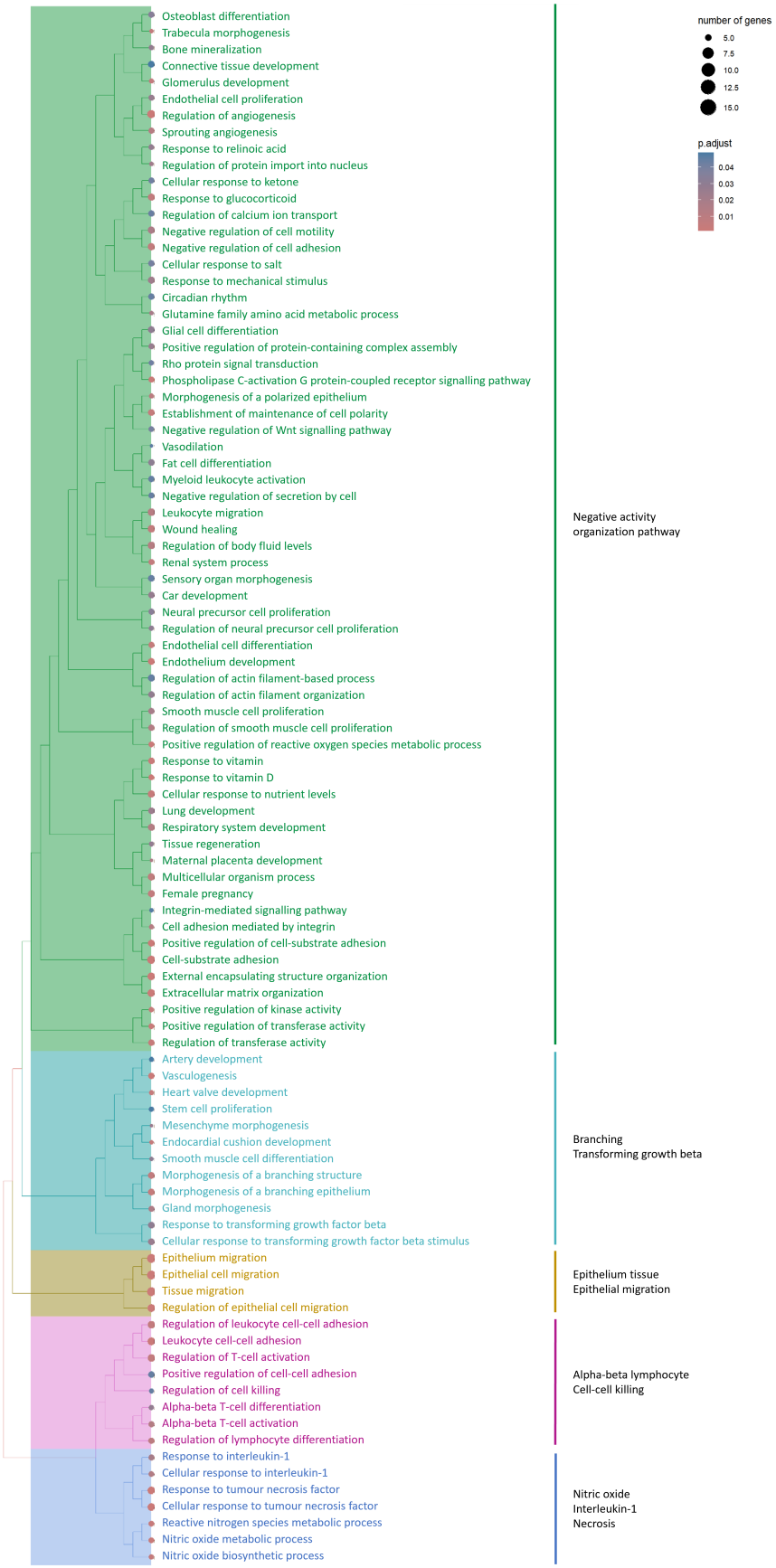
number of genes
5.0
7.5
10.0
12.5
15.0
p.adjust
0.04
0.03
0.02
0.01
Osteoblast differentiation
Trabecula morphogenesis
Bone mineralization
Connective tissue development
Glomerulus development
Endothelial cell proliferation
Regulation of angiogenesis
Sprouting angiogenesis
Response to relinoic acid
Regulation of protein import into nucleus
Cellular response to ketone
Response to glucocorticoid
Regulation of calcium ion transport
Negative regulation of cell motility
Negative regulation of cell adhesion
Cellular response to salt
Response to mechanical stimulus
Circadian rhythm
Glutamine family amino acid metabolic process
Glial cell differentiation
Positive regulation of protein-containing complex assembly
Rho protein signal transduction
Phospholipase C-activation G protein-coupled receptor signalling pathway
Morphogenesis of a polarized epithelium
Establishment of maintenance of cell polarity
Negative regulation of Wnt signalling pathway
Vasodilation
Fat cell differentiation
Myeloid leukocyte activation
Negative regulation of secretion by cell
Leukocyte migration
Wound healing
Regulation of body fluid levels
Renal system process
Sensory organ morphogenesis
Car development
Neural precursor cell proliferation
Regulation of neural precursor cell proliferation
Endothelial cell differentiation
Endothelium development
Regulation of actin filament-based process
Regulation of actin filament organization
Smooth muscle cell proliferation
Regulation of smooth muscle cell proliferation
Positive regulation of reactive oxygen species metabolic process
Response to vitamin
Response to vitamin D
Cellular response to nutrient levels
Lung development
Respiratory system development
Tissue regeneration
Maternal placenta development
Multicellular organism process
Female pregnancy
Integrin-mediated signalling pathway
Cell adhesion mediated by integrin
Positive regulation of cell-substrate adhesion
Cell-substrate adhesion
External encapsulating structure organization
Extracellular matrix organization
Positive regulation of kinase activity
Positive regulation of transferase activity
Regulation of transferase activity
Negative activity
organization pathway
Artery development
Vasculogenesis
Heart valve development
Stem cell proliferation
Mesenchyme morphogenesis
Endocardial cushion development
Smooth muscle cell differentiation
Morphogenesis of a branching structure
Morphogenesis of a branching epithelium
Gland morphogenesis
Response to transforming growth factor beta
Cellular response to transforming growth factor beta stimulus
Branching
Transforming growth beta
Epithelium migration
Epithelial cell migration
Tissue migration
Regulation of epithelial cell migration
Epithelium tissue
Epithelial migration
Regulation of leukocyte cell-cell adhesion
Leukocyte cell-cell adhesion
Regulation of T-cell activation
Positive regulation of cell-cell adhesion
Regulation of cell killing
Alpha-beta T-cell differentiation
Alpha-beta T-cell activation
Regulation of lymphocyte differentiation
Alpha-beta lymphocyte
Cell-cell killing
Response to interleukin-1
Cellular response to interleukin-1
Response to tumour necrosis factor
Cellular response to tumour necrosis factor
Reactive nitrogen species metabolic process
Nitric oxide metabolic process
Nitric oxide biosynthetic process
Nitric oxide
Interleukin-1
Necrosis

955 Figure S10

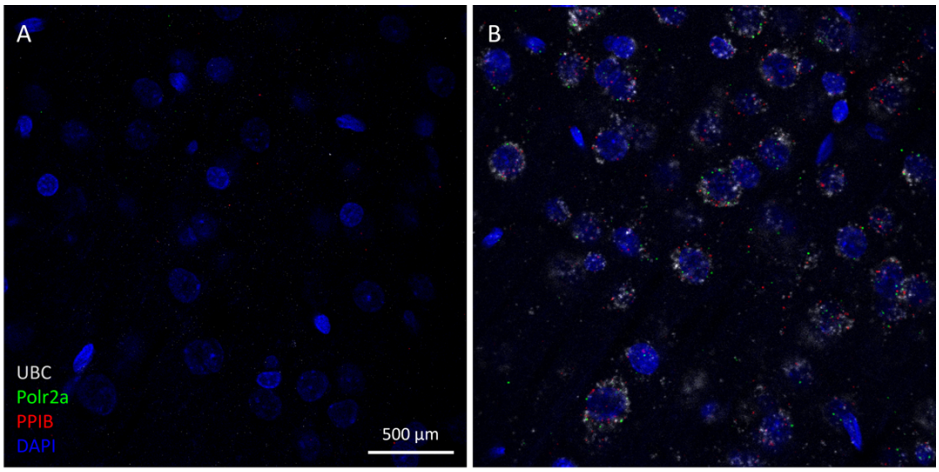

956

957